Gap solitons and forced snaking

Benjamin C. Ponedel and Edgar Knobloch

Phys. Rev. E **98**, 062215 — Published 17 December 2018

DOI: 10.1103/PhysRevE.98.062215

Gap solitons and forced snaking

Benjamin C. Ponedel and Edgar Knobloch
Department of Physics, University of California at Berkeley, Berkeley CA 94720, USA

We introduce the phenomenon known as *forced snaking* to the study of gap solitons and use this notion to identify two distinct bifurcation diagrams organizing such solitons in the semi-infinite gap of the continuous cubic-quintic Gross-Pitaevskii equation with a spatially periodic potential. Standard snaking is found for small interpotential or lattice spacing while foliated snaking is present for large spacing. In each case we determine the stability of the symmetric on-site and off-site solitons and show that multi-soliton solutions of both types are stabilized when the spacing is sufficiently large, effectively quenching the interaction between the solitons. Finally we show that the solitons unbind from the potential when subjected to sufficiently large asymmetric or symmetric perturbations and use direct numerical simulation to investigate their break-up and associated radiative losses as they propagate. A strongly nonlinear theory that captures key aspects of the depinning dynamics is provided.

I. INTRODUCTION

Discrete solitons have been the subject of intense study in nonlinear optics since their prediction in 1988 [1, 2]. A particular type of soliton known as the "gap soliton," first proposed in 1994 [3], arises amidst a competition between nonlinear self-focusing effects and anomalous diffraction in periodic waveguides. These structures are typically modeled using a nonlinear Schrödinger equation (NLSE) in the presence of an external periodic potential, i.e., the Gross-Pitaevskii equation (GPE). An enormous amount of theoretical work has been done on the structure and stability of solutions to this model for a variety of nonlinearities, e.g. [4–6]. More recently an effort has been made to understand solutions referred to as multipole solitons or soliton complexes that involve arrays of nearly identical solitons pinned to the periodic potential [5, 7–11]. Related work has investigated multipulse solutions in a cubic-quintic medium in which the solution possesses a finite set of identical maxima but is not composed of isolated solitons [5, 12–14]. Our work connects these two distinct types of structures providing a unified picture of how they relate to one another in the cubic-quintic case and elucidates their stability properties.

The simplest models for optical solitons describe a Kerr medium resulting in a NLSE with a cubic nonlinearity. More complex nonlinearities arise in other systems, however, and cubic-quintic nonlinearities in particular have been observed in a plethora of experiments [15–19]. These are the subject of the present paper. In the presence of an externally imposed spatially periodic potential $V(x)$ the resulting cubic-quintic GPE takes the form

$$-iA_t = A_{xx} - V(x)A + |A|^2A - |A|^4A. \tag{1}$$

This is an equation for a complex-valued order parameter $A(x,t)$. In the following we focus on the case of a sinusoidal potential $V(x) = -m_1\cos(2\pi x/\ell)$ and use the parameter m_1 to change its amplitude and the parameter ℓ to vary its period or equivalently the "lattice spacing" in the language of discrete NLS models. In the following we focus exclusively on solutions of the form $A(x,t) = e^{-im_0t}u(x)$ describing a standing oscillation with a fixed albeit nonuniform spatial profile and a rotating phase. Such states are solutions of the nonlinear ordinary differential equation (ODE)

$$\begin{aligned} 0 &= u_{xx} + \left[m_0 + m_1\cos\left(\frac{2\pi x}{\ell}\right)\right]u + |u|^2u - |u|^4u \\ &\equiv u_{xx} + \mathcal{N}(u,x). \end{aligned} \tag{2}$$

This equation takes the form of the cubic-quintic Ginzburg-Landau equation (GLE) with a periodically oscillating bifurcation parameter and has been studied in this context in [20]. Here we are interested in particular in spatially localized solutions of this equation, i.e., in solitary wave solutions of the GPE. Such solutions are frequently called solitons (a custom we follow below) although they are not true solitons, i.e., solutions of a completely integrable partial differential equation (PDE).

To determine solitary wave solutions of Eq. (1) one must understand the (spatial) linear dispersion relation around the trivial solution $u = 0$ of Eq. (2). Because the linear problem is periodically forced it is described by Floquet theory and possesses a characteristic band-gap structure. Specifically, the Floquet exponents for the linear problem only have a nonzero real part in certain regions of the (m_0, m_1) parameter plane and are otherwise purely imaginary. These regions in the (m_0, m_1) plane are referred to as band-gaps and are shown in white in Fig. 1. For parameters in these regions $u \equiv 0$ is a hyperbolic fixed point of Eq. (2) and the ODE can therefore support solutions that are homoclinic to $u = 0$. These solitary wave solutions are colloquially referred to as gap solitons.

For fixed m_1 the band structure (white regions in Fig. 1) takes the form of a countable set of intervals in m_0. The first of these intervals, $-\infty < m_0 < m^*(m_1)$, is of infinite extent and is called the semi-infinite gap. All higher gaps are finite open intervals. In the following we study gap solitons restricted to the semi-infinite gap in which the ODE (2) has two simultaneously hyperbolic

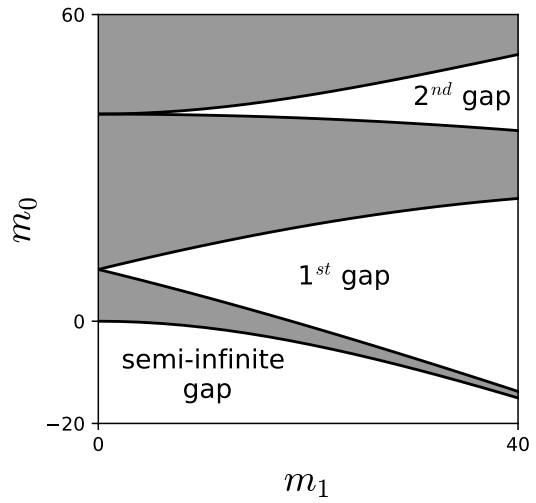

FIG. 1. The band-gap structure in the (m_0, m_1) plane for the lowest three gaps of the linearization of Eq. (2). Solutions that are homoclinic to $u \equiv 0$ (equivalently $A \equiv 0$) represent solitons and exist only within the band gaps (white regions in the diagram).

fixed points. These two solutions are $u(x) = 0$ and a periodic solution with period ℓ, the period of the externally imposed potential. In previous work [20] we showed that Eq. (2) exhibits a phenomenon we called forced snaking that is responsible for the presence of multiple families of spatially localized solutions which we interpret here in terms of gap solitons of the GPE. Some of the solutions in [20] appear in earlier work [5, 14].

Homoclinic snaking [21, 22] is present in both discrete [13, 23–26] and continuous [14, 27–30] models of optical systems. This term describes the origin and properties of a large or infinite multiplicity of spatially localized structures present within an interval of parameter values, a phenomenon exemplified in the optics literature by the Lugiato-Lefever equation [30], a complex-valued equation for the amplitude of the (transverse) electric field in a continuously pumped optical cavity. This equation is of second order in space and consequently its stationary states solve a fourth order real-valued ODE which supports standard homoclinic snaking, eg., [27, 29, 31]. In contrast, the focus of this paper is on snaking that results from imposed periodic spatial modulation, i.e., on *forced* snaking.

Some of our results for larger m_1, i.e., greater potential depth, resemble those obtained from discrete models of optical systems, and specifically those obtained by Chong and Pelinovsky for the discrete cubic-quintic NLSE [26]. Models of this type are typically derived from a continuum formulation in the tight binding approximation where the potential depth diverges, $m_1 \to \infty$ [32]. In the discrete system that results the original parameters m_1 and ℓ replaced by a single parameter, often referred to as C. The discrete system models the amplitude at each lattice site, i.e., the amplitude of the spatial modes trapped in the different wells of the potential. Although the behavior of the continuous and discrete systems is in some cases similar, the fact remains that the tight-binding assumption leads to the loss of one of the system parameters and the discrete formulation can therefore only capture a subset of the behavior described by the continuum formulation.This paper focuses on exploring the behavior of the continuum system far from the discrete NLSE limit, i.e., for modest values of the parameter m_1. We show that in this regime the lattice spacing ℓ plays a fundamental role and is responsible for the presence of a new bifurcation diagram organizing gap solitons at large enough ℓ.

This paper is organized as follows. In Section II we briefly summarize the bifurcation structure of the solutions in our previous work [20] and explain the phenomenon of forced snaking. We also show that the spatial scale of the potential, ℓ, has a major impact on the bifurcation structure of these solutions, and use the values $\ell = 10$ and $\ell = 50$ to illustrate two distinct regimes. In Section III we compute the linear stability of the snaking solutions and in Section IV we use the results to investigate the dynamics and break-up of unstable solutions, focusing on the new, large ℓ regime. The paper concludes with a discussion in Section V. In Appendix A we report on a strongly nonlinear theory that captures the essence of the depinning behavior leading to soliton mobility. Appendix B details our numerical methods.

II. FORCED SNAKING

For fixed parameters Eq. (2) possesses multiple multipulse solutions. As a function of the parameter m_0 these solutions lie on a countable set of distinct bifurcation curves. In [20] we term this behavior *forced snaking*. These localized solutions are real-valued despite Eq. (2) admitting complex solutions. To see this we write $u(x) = r(x)e^{i\phi(x)}$ yielding

$$r_{xx} - r\phi_x^2 - V(x)r + r^3 - r^5 = 0$$
$$\frac{d}{dx}\log\left(r^2\phi_x\right) = 0. \tag{3}$$

Integrating Eq. (3) once leads to $\phi_x = Kr^{-2}$, implying that $r_{xx} - K^2r^{-3} - Vr + r^3 - r^5 = 0$. When $K \neq 0$ this equation does not admit solutions that are homoclinic to $r = 0$, i.e. to $u = 0$, implying that such states are only possible when $K = 0$ and that ϕ is therefore constant. Without loss of generality we take $\phi = 0$.

The details of this bifurcation structure depend significantly the three parameters m_0, m_1 and ℓ characterizing the equation. In the following we summarize the main results concerning localized states in Eq. (2). These fall into two distinct regimes depending on the lengthscale of the forcing, ℓ, and in each case are analyzed in stages as we increase the potential depth, m_1, from zero.

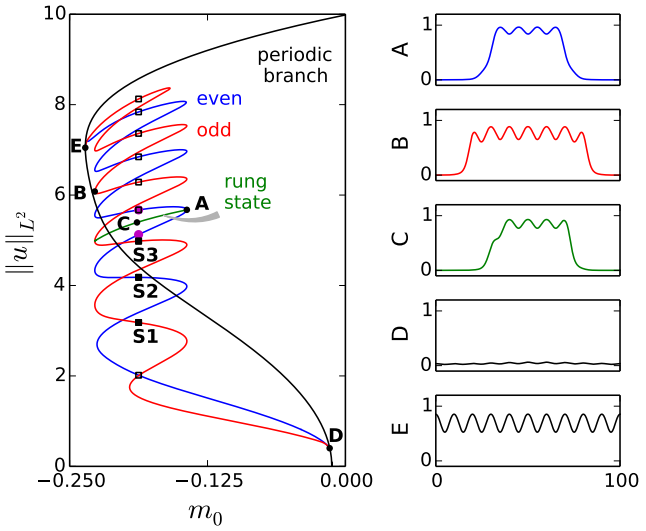

FIG. 2. Bifurcation diagram showing periodic and localized states when $m_1 = 0.1$, $\ell = 10$ on a periodic domain. The latter are organized within a classical snakes-and-ladders structure [21, 22] and consist of states with N bumps: states with N even (odd) are found on the blue (red) snaking branch. Connecting each pair of folds is a branch of asymmetric rung states (green) only one of which is shown. The snaking branches bifurcate together from (and reconnect together to) a domain-filling periodic state. Plots on the right show solutions $u(x)$ at points marked with (•), shown over the full domain $0 \le x \le 100$. Solutions labeled with (□, ■) have $m_0 = -\frac{3}{16}$ and are relevant to the stability calculations (Fig. 6) and time simulations shown below. Solutions marked with magenta circles are shown explicitly in Fig. 3.

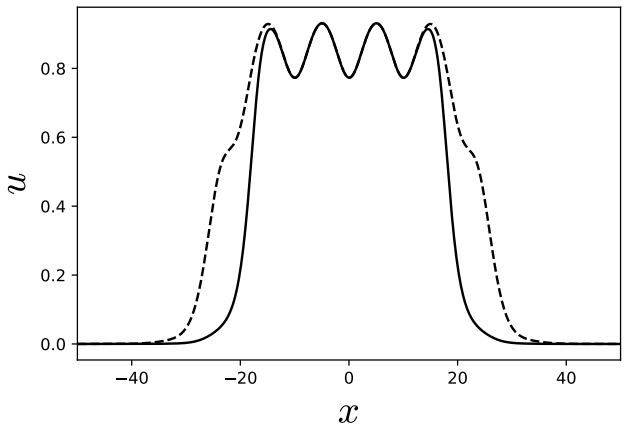

FIG. 3. Two successive 4-bump snaking solutions at $m_0 = -\frac{3}{16}$, $m_1 = 0.1$, $\ell = 10$. The stable solution is drawn with a solid line and the unstable one with a dashed line (see section II). These solutions correspond to the magenta points in Fig. 2.

A. Short-scale forcing, $\ell = 10$

For small values of ℓ the addition of periodic parametric forcing to the GLE model produces localized states that exhibit classic snaking. The addition of parametric forcing on a short lengthscale (here $\ell = 10$) causes the constant amplitude solutions on the primary branch of the GLE to become periodic with the same period as the forcing. Figure 2 shows a pair of intertwined branches of localized states that bifurcate from the newly periodic primary branch at low amplitude (location D) and enter a pinning region as they are continued in the parameter m_0, exhibiting snaking, before terminating on a branch of domain-filling periodic states (location E). The solutions on these branches are characterized by the number N of bumps of the periodic state contained within them. This number can be either odd or even. Each back and forth excursion of the solution branch across the pinning region results in the addition of one new bump on either side the solution thereby maintaining the parity of N. In addition, a set of spatially asymmetric "rung" states connects opposite folds on the snaking branches. Only one rung is shown in the figure. This structure does not change qualitatively when m_1 is increased.

Each N-bump solution occupies two consecutive sections of the snaking branch separated by a fold on the right, a lower section with a larger slope and an upper one with a smaller slope (Fig. 2). Figure 3 shows a pair of solutions, the dashed line from an upper section and the solid line from the previous lower section, both at the same parameter value, showing the process whereby the folds on the right are responsible for the appearance of an extra pair of pre-bumps on either side. The center parts of the solutions are the same. As m_0 decreases the pre-bumps grow into full bumps turning the state into a $N + 2$-bump solution.

The asymmetric rung branches can be understood in terms of this dichotomy. Rung states, like the one shown in Fig. 2, are made up one half of the dashed solution and one half the solid solution shown in Fig. 3. As they are continued in m_0 the structure gains a single full bump on one side and thus changes parity (N bumps to $N + 1$). Thus rung branches connect opposite folds on the odd and even branches. Previous work on "symmetry breaking" in gap-soliton systems [26, 33] has found similar asymmetric solutions.

B. Long-scale forcing, $\ell = 50$

For larger values of the forcing wavelength or "lattice spacing" ℓ localized states persist but are no longer arranged in the classical snakes-and-ladders structure shown in Fig. 2. As documented in [20], the bifurcation structure of the localized states now depends more strongly on m_1. For small m_1 classical snaking is observed but at a moderate value, here $m_1 \approx 0.035$ with $\ell = 50$, the snaking structure breaks down entering a regime that we have termed "foliated snaking." An example of this scenario is pictured in Fig. 4 in which we plot

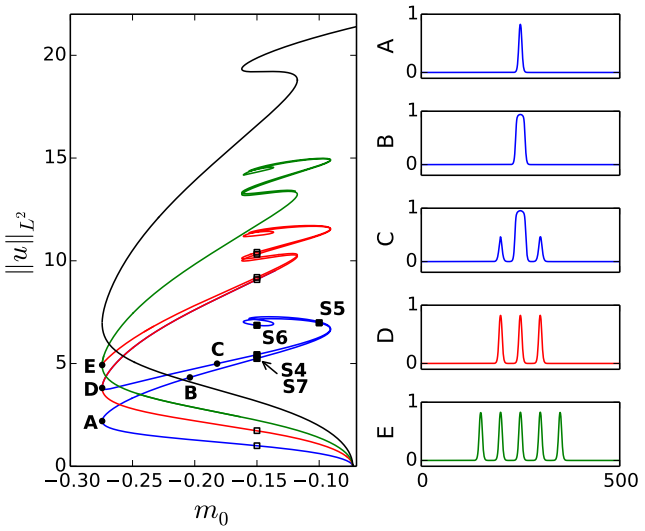

FIG. 4. Bifurcation diagram for $m_1 = 0.1$ when $\ell = 50$ showing FPT branches based on one spike (blue), three spikes (red) and five spikes (green). The periodic branch is shown in black. The branches interconnect at the left folds. Panels on the right show solutions $u(x)$ at points marked with (•), shown over the full domain $0 \le x \le 500$. Solutions labeled with (□, ■) have $m_0 = -0.15$ or $m_0 = -0.1$ and are relevant to the stability calculations (Fig. 7) and time simulations shown below.

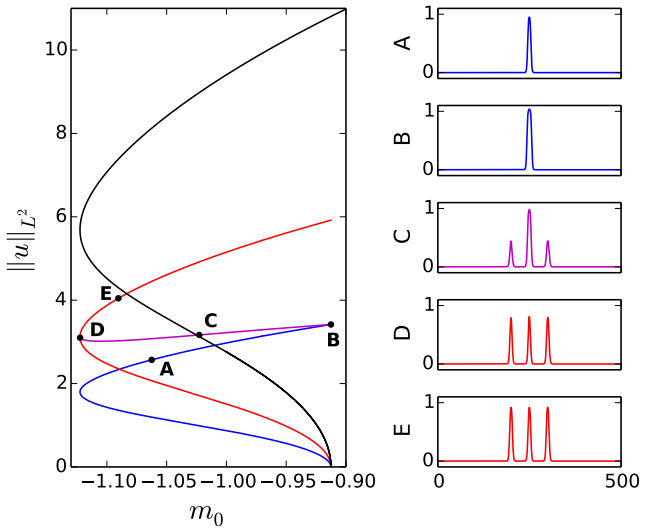

FIG. 5. Bifurcation diagram for $m_1 = 1$ when $\ell = 50$ showing FPT branches based on one spike (blue) and three spikes (red) emanating from the primary bifurcation and a mixed PT branch consisting of one lump and two spikes (magenta) connecting the two. The periodic branch in shown in black. Sample solution profiles are shown on the right.

soliton states taking the form of finite pulse trains (FPT), with an odd number of peaks. Similar states consisting of a finite even number of solitons are also present. In the foliated snaking regime soliton branches with odd/even number of peaks maintain parity-preserving interconnectivity, but the bifurcation diagram is significantly different. This is because the FPT states may sample solitons from either the upper (lump) or the lower (spike) branch of periodic states (black curve in the figure) resulting in FPT with all possible combinations of lumps and spikes, with gaps ($u = 0$) permitted. The lumps and spikes are located at the cosine maxima (i.e., minima of $V(x)$, as expected). Because of the up-down symmetry, $u \to -u$, states with negative (i.e., dark) lumps are also present. Thus FPT consisting of a mix of bright and dark solitons are possible, although these are not considered here.

All branches of localized states with spikes bifurcate from the primary bifurcation point at $m_0 = m_c$ and initially take the form of a pulse train with N spikes. As they are continued in m_0 the branch passes the leftmost fold thereby turning the spikes into lumps. Upon further continuation the lump state undergoes a complicated set of bifurcations that ultimately add a pair of spikes, one at either edge of the structure, and allow the branch of N lumps to connect to that with $N + 2$. In principle arbitrary combinations of spikes and lumps can be combined to form localized states indicating that the complete bifurcation diagram is in fact much more complicated. Here we only consider states formed by either N spikes or N lumps that are adjacent to each other. The reader is referred to [20] for more details about the emergence of this bifurcation structure and the details of the spike-adding process.

The above scenario becomes yet clearer at larger m_1 when the rightmost folds collide with $m_0 = m_c$. Figure 5 shows the results for $m_1 = 1$. Like the lower m_1 value, pulse trains can be constructed with either a lump, spike or $u = 0$ at each cosine maximum and thus one can construct families of soliton states. A FPT with N lumps and M spikes when continued in m_0 below m_c turns around at the left fold on the branch of periodic states. At this fold the lumps and spikes coincide but as m_0 increases back towards m_c any spikes in the structure shrink to $u \equiv 0$. Thus a 1-lump, 2-spike solution coincides with a 1-lump solution when $m_0 = m_c$ and the two branches meet in what is effectively a cusp.

The presence of the cusp is indicative of the separation of scales in Eq. (2). Between the bumps the ODE solution is exponentially small (a property that is exacerbated as ℓ increases) and the nonlinear terms in Eq. (2) are therefore even smaller while the potential is $\mathcal{O}(1)$. Thus to high accuracy the solution between the bumps may be taken to be $u = 0$. This means that the localized soliton states behave as independent concatenations of lumps and spikes rather than a single family: the nonlinear terms do couple the bumps, but do so exponentially weakly. The cusps that are observed in the bifurcation diagram are thus expected to be blunt upon close inspection, but with curvature inversely related to the exponentially small coupling between the pulses.

The presence of two distinct bifurcation diagrams or-

ganizing gap solitons on the GPE is a significant new result. Existing work on the discrete cubic-quintic NLSE has identified the scenario in Fig. 2, i.e., classical snaking, but to the authors' knowledge the foliated snaking scenario (Fig. 5) has not been seen in either the discrete NLSE or the GPE. It is, however, documented in studies of the ac-driven, damped nonlinear Schrödinger equation [34].

III. STABILITY

The linear stability of the solution $A(x,t) = e^{-im_0 t}u(x)$ of Eq. (1) may be studied using the Ansatz

$$A(x,t) = e^{-im_0 t}(u(x) + [a(x)+b(x)]e^{\sigma t} + [a^*(x)-b^*(x)]e^{\sigma^* t})$$

followed by linearization in the complex amplitudes a and b. This procedure leads to a linear eigenvalue problem for the growth rate σ:

$$-i\sigma \begin{pmatrix} a \\ b \end{pmatrix} = \begin{pmatrix} 0 & \partial_{xx} + \tilde{\mathcal{N}}(u,x) \\ \partial_{xx} + \mathcal{N}_u(u,x) & 0 \end{pmatrix} \begin{pmatrix} a \\ b \end{pmatrix} \equiv \mathcal{L} \begin{pmatrix} a \\ b \end{pmatrix}. \tag{4}$$

In writing this equation we have assumed that $u(x)$ is real-valued, with $\tilde{\mathcal{N}}(u,x) \equiv \mathcal{N}(u,x)/u$, $\mathcal{N}_u(u,x) \equiv \partial_v \mathcal{N}(v,x)|_{v=u}$ and $\mathcal{N}$ defined as in Eq. (2). We solve this eigenvalue problem using a Fourier pseudo-spectral method details of which are discussed in Appendix B. This eigenvalue problem has the null eigenfunction $(a,b) = (0,u)$ with algebraic multiplicity 2. The multiplicity of the eigenvalue can be seen by differentiating $u_{xx} + \mathcal{N}(u,x) = 0$ with respect to m_0 yielding the identity

$$-\left[\partial_{xx} + \mathcal{N}_u(u,x)\right] \frac{\partial u}{\partial m_0} = u \tag{5}$$

from which it follows that $\partial_{m_0} u$ is a generalized eigenfunction with eigenvalue 0. The presence of the potential breaks translation invariance which would otherwise generate an additional null eigenfunction.

When $\sigma \neq 0$ this eigenvalue problem can be diagonalized, viz. $\sigma^2 a = -\left[\partial_{xx} + \tilde{\mathcal{N}}(u,x)\right]\left[\partial_{xx} + \mathcal{N}_u(u,x)\right] a$. From reflection symmetry it is clear that if σ is an eigenvalue of this equation, then $-\sigma$ and $\pm\sigma^*$ are eigenvalues also. Thus stable solutions have a spectrum entirely confined to the imaginary axis. Instabilities occur when eigenvalues exit the imaginary axis into the right half-plane. If these eigenvalues have zero imaginary part the instability is known as an exponential instability; otherwise it is an oscillatory instability (OI). In this work we have only found exponential instabilities; however, the occurrence of OI can be subtle [35] and eigenvalues may have very small real parts. We leave a careful study of OI to future work. In the diagonalization performed here $\sigma^2 > 0$ corresponds to a pair of eigenvalues on the real axis, symmetric about $\sigma = 0$, whereas $\sigma^2 < 0$ corresponds to a pair of symmetrically disposed eigenvalues on the imaginary axis. Since the diagonalized eigenvalue problem may not capture all of the zero eigenvalues that are present we check the results by computing the nullspace of the operators $\partial_{xx} + \tilde{\mathcal{N}}(u,x)$ and $\partial_{xx} + \mathcal{N}_u(u,x)$ as well.

A. Short-scale forcing, $\ell = 10$

Stability results for forced snaking solutions replicate known results at low amplitude and exhibit stability switching at folds higher up on the snaking branch. In Fig. 6 we plot curves of the squares of the three largest eigenvalues, σ^2, as a function of the arclength s along the two branches of snaking solutions measured from the bottom. These are computed by calculating the entire eigenspectrum for a series of solutions along the bifurcation curve. Folds on the solution branches are denoted by grey vertical dotted lines at the associated location s. The continuation is initiated at low amplitude (point D in Fig. 2) where the branch with an odd (even) number of bumps is stable (unstable). In the even case the branch restabilizes before the first fold is reached but no stability change occurs in passing the first fold on the odd branch. Despite this behavior at the lowest folds subsequent folds do coincide with stability switching for the snaking solutions. Most of the unstable segments of each branch are in fact unstable with respect to an additional unstable eigenvalue as well that leaves the imaginary axis and returns to it between the folds. However, the real part of

this second eigenvalue is strictly smaller than that of the primary one and is thus of little dynamical importance. As can be seen by the ordering of eigenvalues in the figure no other eigenvalues go unstable in traversing either branch.

The decorrelation between stability switching and the location of the folds is a consequence of the structure of the temporal stability eigenvalue problem for solutions of the GPE as explained in [36]. In this paper the author shows that for a large class of NLS-type equations the algebraic multiplicity of the 0 eigenvalue does not change at fold bifurcations in the ODE (2). Thus, no eigenvalues can escape into the right half-plane. Instead, the effect of the 0 eigenvalue of the operator $\partial_{xx} + \mathcal{N}_u(u, x)$ is to change the geometric multiplicity of the 0 eigenvalue of $\mathcal{L}$. Specifically, at the fold bifurcation the identity (5) is invalid and the eigenvalue 0 does not have any generalized eigenfunctions [36]. However, the algebraic multiplicity of the zero eigenvalue of $\mathcal{L}$ is preserved by the presence of a "fold eigenfunction" of the operator $\partial_{xx} + \mathcal{N}_u(u, x)$. The effect on the 0 eigenspace of $\mathcal{L}$ can be thought of as a change between the following Jordan blocks:

$$\begin{pmatrix} 0 & 1 \\ 0 & 0 \end{pmatrix} \to \begin{pmatrix} 0 & 0 \\ 0 & 0 \end{pmatrix}.$$

The "fold eigenfunction" is intimately related to the divergence of the function $\partial_{m_0} u$ as the fold $m_0 = m_F$ is approached, $\partial_{m_0} u \approx (m - m_F)^{-\frac{1}{2}}$. Multiplying the identity (5) by $\sqrt{m - m_F}$ before taking the limit shows that $\partial_{m_0} u$ passes smoothly into an eigenfunction of the operator $\partial_{xx} + \mathcal{N}_u(u, x)$ at m_F. Of course this mechanism does not preclude additional eigenvalues passing through 0 at folds in the ODE but it does not mandate it. For a rigorous treatment of this argument we direct the reader to Ref. [36].

The character of the instabilities and the failure to switch stability at the first folds can be gleaned from the structure of the associated stationary state and its eigenfunctions. Figure 6 shows the two eigenfunctions corresponding to the most unstable eigenvalues (black and blue) at arclength locations marked by open circles. These points were chosen all to be at the parameter value $m_0 = -\frac{3}{16}$ so that the periodic state is the same in all cases. Because the eigenvalues observed here are all real the Ansatz (4) for the perturbations is too general and we find that $a(x)$ is purely real while $b(x)$ is purely imaginary. We thus plot $\Re(a)$ with a solid line and $\Im(b)$ with a dashed line in each subplot. In a few cases $\Re(a) \equiv 0$ and is omitted. In each case the corresponding base state is shown in grey. All of the subplots in each row have a consistent vertical scaling so the amplitudes of the nonlinear states can be compared. The largest eigenvalue for the unstable states corresponds to an eigenmode (black) that is antisymmetric across the structure with $a(x)$ localized at the structure boundaries. This type of edge-localized mode is observed in classical snaking systems. However, because the corresponding $b(x) \not\equiv 0$ this mode also rotates the real-valued stationary state $u(x)$ into a fully complex and hence dynamic state. This behavior is in fact violated by the last state on the odd branch since this localized state is now so broad that it reaches the boundary of the domain. When the domain has an even number of cosine wavelengths (say 10) the final branch segment on the odd branch (a state of size 9) has a most unstable mode of even parity, localized on the only remaining unoccupied spot. We expect a similar violation for the even branch when the domain spans an odd number of cosine wavelengths but no such violation when the problem is posed on the real line.

When there is a second unstable eigenvalue, the associated eigenmode is symmetric across the structure. This mode thus corresponds either to growing or shrinking of the structure depending on the sign of $a(x)$. As in classical snaking, this mode takes the solution to the branch segment above or below in the snaking structure by growing or shedding the bumps at both boundaries of the structure simultaneously. However, because the associated $b(x)$ is again nonzero the resulting solution becomes fully complex and hence also time-dependent. Which mode is selected depends of course on the nature of perturbation around the stationary state.

The symmetric mode is not always unstable, however, and remains stable along the first instability intervals on both branches. We believe that this nonuniversal behavior, just like the decorrelation between the first folds and stability switching, is a consequence of the small spatial extent (and hence small norm) of the soliton states in this regime. Similar pre-localized behavior near the base of the snaking branches is present in classical snaking as well and causes the small-norm solutions to have different properties from their more spatially extended brethren higher up on the branch.

B. Long-scale forcing, $\ell = 50$

In the foliated snaking regime the stability results are considerably different. Figure 7 shows the squares of the largest eigenvalues, σ^2, for the 1-lump and 3-lump foliated snaking branches (blue and red branches from Fig. 4). The 1-lump branch is stable except during pulse addition, i.e. between its second and last fold, where it is unstable. This instability is the result not only of eigenvalue crossings at the folds but of additional crossings inside the instability interval as well. The 3-lump branch has a similar structure with all the instability intervals associated with the pulse addition process. The most remarkable feature of these results is that stability switching does not occur at the spike-lump fold and that pulse trains with both spikes and lumps are stable. This is in significant contrast to the dissipative case studied in [20] where spikes are always unstable.

Solutions with N lumps and M spikes have a multiplicity $N + M$ zero eigenvalue. The intuition for this is as follows. The null eigenfunction $(a, b) = (0, u)$ is local-

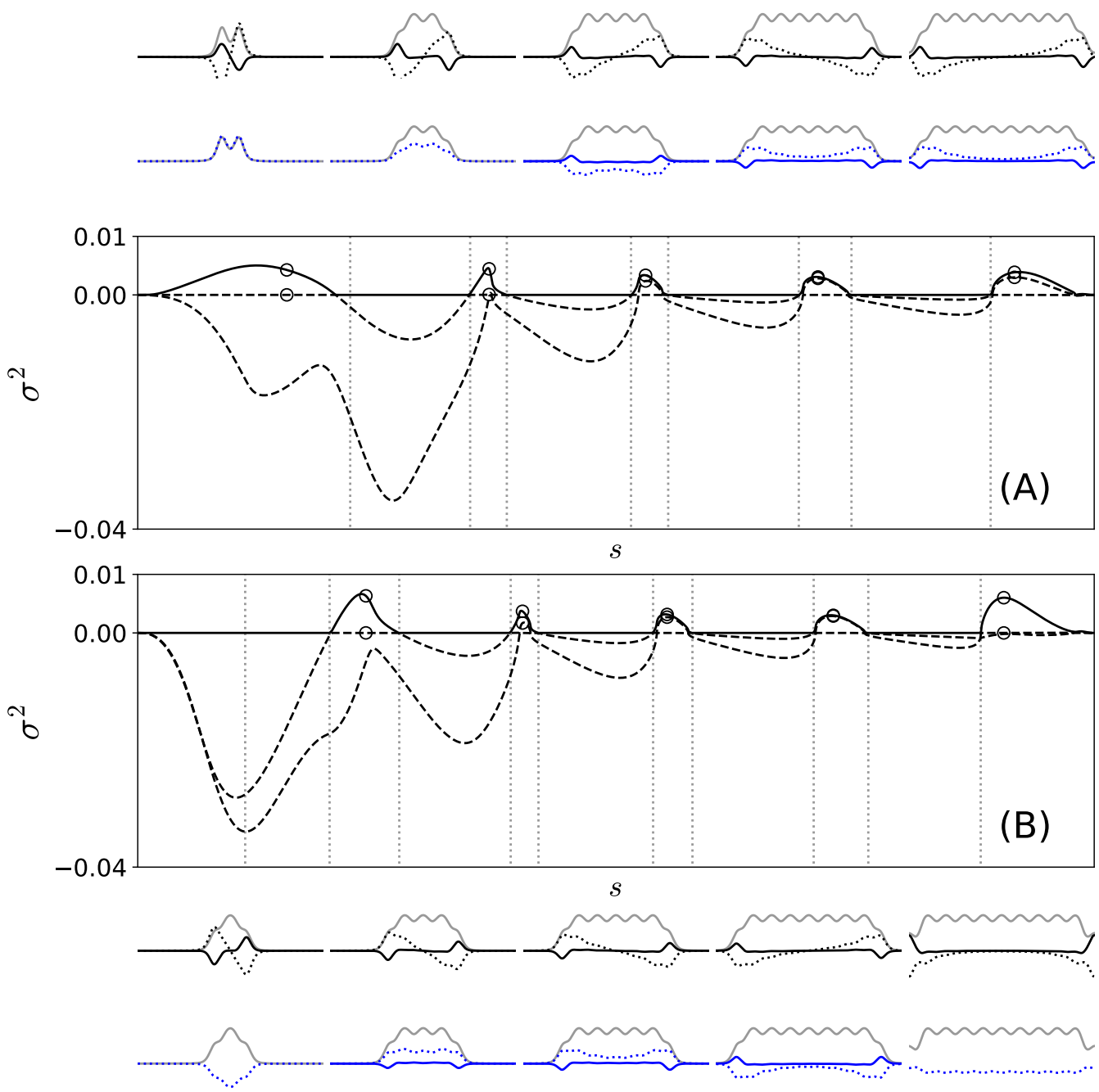

FIG. 6. The three largest linear stability eigenvalues σ^2 for the solutions in Fig. 2 computed as a function of the arclength s. The largest eigenvalue σ^2 is plotted using a solid black line while all smaller eigenvalues are shown using a dashed line. Inset (A) represents a branch of solutions with an even number of bumps while inset (B) represents a branch with an odd number. Specific base states at $m_0 = -\frac{3}{16}$ (grey) and the corresponding eigenfunctions (largest eigenvalue in black, second largest eigenvalue in blue) of the even-bump branch are plotted above (A) with the corresponding results for the odd-bump branch shown below (B). In each case the real part $\Re[a(x)]$ of the eigenfunction is shown using a solid line while the imaginary part $\Im[b(x)]$ is plotted using a dotted line. In some cases $a(x) \equiv 0$ and we omit it from the eigenfunction plot. In each case the open circles (which may overlap) indicate the location of the base states used to compute the eigenfunctions shown.

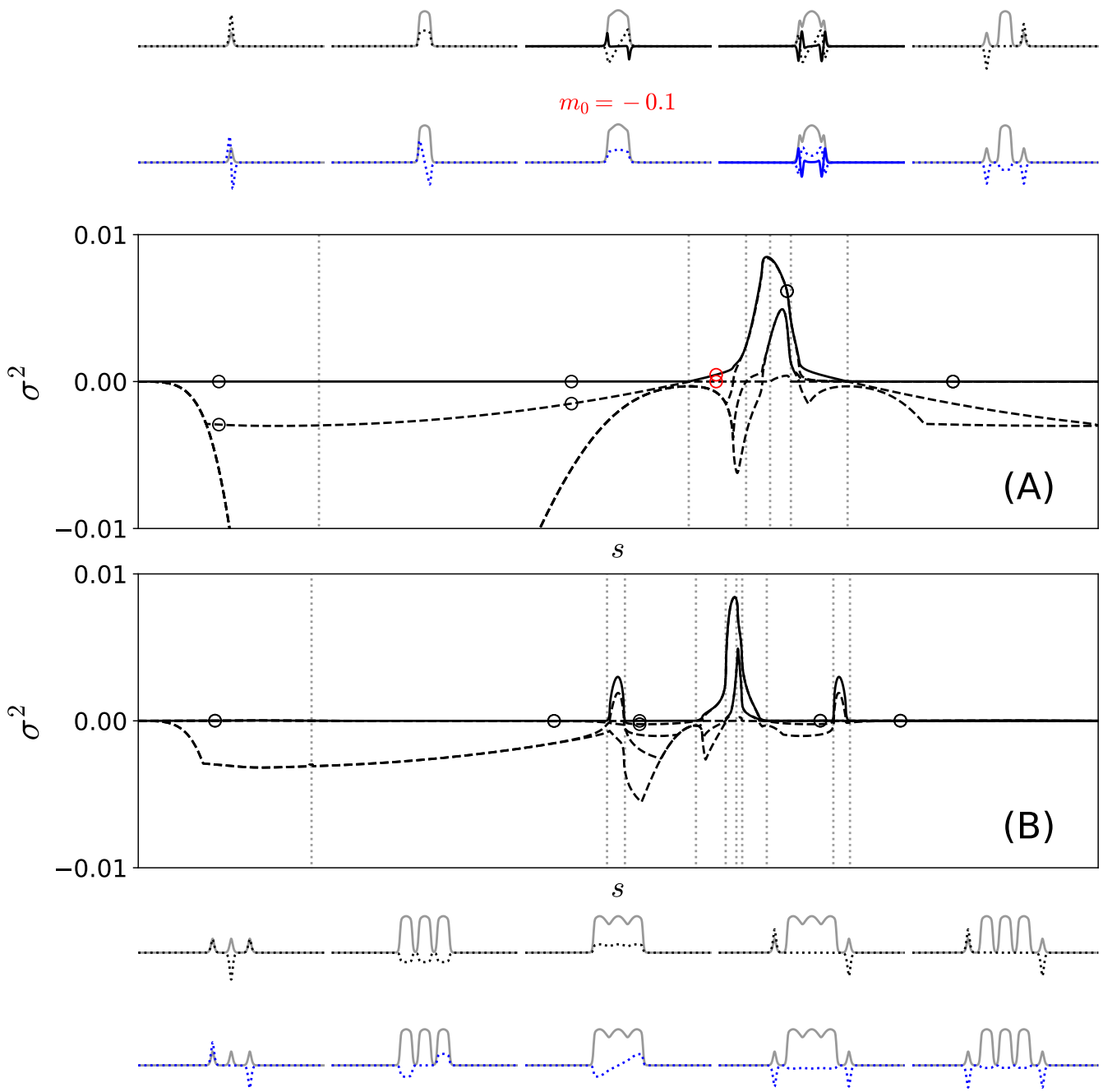

FIG. 7. The five largest linear stability eigenvalues σ^2 for the solutions in Fig. 4 computed as a function of the arclength s. The largest eigenvalue σ^2 is plotted using a solid black line while all smaller eigenvalues are shown using a dashed line. Inset (A) represents the single pulse FPT branch while inset (B) represents the three-pulse FPT branch. Typical base states (grey) and eigenfunctions (largest eigenvalue in black, second largest eigenvalue in blue) on the branch with an even number of bumps are plotted above (A) with the corresponding results for the branch with an odd number of bumps shown below (B). In each case the real part $\Re[a(x)]$ of the eigenfunction is shown using a solid line while the imaginary part $\Im[b(x)]$ is plotted using a dotted line. In some cases $a(x) \equiv 0$ and we omit it from the eigenfunction plot. The states are mostly computed at $m_0 = -0.15$ (except for the one marked in red); their location is indicated using open circles (which overlap when an eigenvalue is degenerate). The second apparently continuous black line in the busy part of panels (A) and (B) is generated by an overlap between a pair of dashed curves. Observe that in both cases the most unstable mode switches from an even parity mode to an odd parity mode as s increases.

ized at the position of the solution. In a finite pulse train the solution nearly vanishes between the lumps or spikes and therefore the nullspace can be parametrized by linear combinations of the eigenfunctions $(0, u_k)$, where u_k is the null eigenfunction corresponding to a solitary lump or spike positioned at the kth cosine maximum.

IV. DYNAMICS

In order to validate our stability calculations and determine the effects of perturbations to the stationary snaking states we turn to time evolution of Eq. (1). These simulations are executed in a rotating frame, that is, we set $A(x,t) = e^{-im_0 t}u(x,t)$ and study the evolution of $u(x,t)$. Details of the numerical implementation are documented in Appendix B. Equation (1) has a number of conserved quantities including an "energy"

$$\mathcal{E} \equiv \int_\Omega |u_x|^2 - \left[m_0 + m_1 \cos\left(\frac{2\pi x}{\ell}\right)\right]|u|^2 - \frac{1}{2}|u|^4 + \frac{1}{3}|u|^6\, dx, \tag{6}$$

where Ω is the system domain, as well as the L^2 norm or "power" of the solution. We refer to the integrand of Eq. (6) as the *energy density* $E(u)$ of the solution. Because of these conserved quantities it is often difficult to simulate dynamics on the real line if the solution radiates energy. When the domain is unbounded radiation may escape to infinity and though energy is conserved globally local dynamics appear to be dissipative [37, 38]. In simulations of this type it is popular to replace the real line by a finite interval with artificial damping imposed at the boundaries. We elected not to do this since there is no well-established method for imposing the damping and incorrect methods will result in unphysical reflected waves that interfere with the solution. For the simulations performed here we chose periodic boundary conditions without any artificial damping. This choice allows us to make precise statements about the time evolution of structures on a periodic domain.

This section is divided into three parts. We first focus on the linear dynamics associated to gap soliton solutions, i.e., the time evolution of gap solitons subjected to *small* perturbations. We observe that a perturbed unstable gap soliton typically evolves into a coherent state that oscillates around a distinct stable stationary gap soliton. This observation leads to the second part of the section in which we describe a set of strongly nonlinear dynamics of perturbed stable gap solitons. We report a pair of *unbinding* phase transitions (or *depinning* bifurcations) in which perturbed stable gap solitons transition from being bound (pinned) by the periodic potential and confined in space, to having sufficient energy to propagate in space. These transitions are strongly nonlinear because they require $\mathcal{O}(1)$ perturbations. Aspects of these results are also supported by an asymptotic theory described in Appendix A in which we show that the dynamics are well described by two degrees of freedom. The third section ties these two parts together. We first show that the bound coherent states arising from perturbed linearly stable and unstable gap solitons can be mapped onto the theory we develop in Appendix A. We also show that the theory accurately describes one of the unbinding transitions.

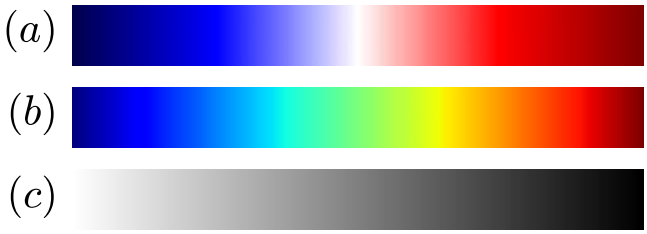

FIG. 8. Color maps used in space-time plots of the solutions in subsequent figures: (a) $|u|$, (b) $\Re(u)$ and (c) $E(u)$.

All of the time simulations performed here are done using the same basic set of parameters. The time integration is performed with a split-step method (see Appendix B) with $n = 1000$ spatial grid points and a time step $dt = 0.001$. The method is pseudo-spectral and periodic boundary conditions are adopted. The energy $\mathcal{E}$ of the solution is well conserved during all of the time simulations, varying at most on the order 10^{-9}. To present the time evolution results we have elected to show three solution measures: the amplitude $|u|$ of the solution, its real part $\Re(u)$ and its energy density $E(u)$. Since each of these solution measures has very different scales we plot them with three distinct color maps that are kept consistent throughout the paper. Because the exact amplitude of the solution is not informative we omit an explicit color bar from the time simulation figures and instead exhibit the ranges for the color maps in Fig. 8 so that maximal and minimal values can be discerned.

A. Linear dynamics of gap solitons

Time simulation of snaking solutions for $\ell = 10$ replicate known results for low amplitude gap solitons in the semi-infinite gap. We confirmed through the linear stability calculation in Fig. 6 and by time-stepping snaking solutions of Eq. (1) the well-known result that the 1-bump branch is stable and the 2-bump branch is unstable near the primary bifurcation [39]. Owing in part to energy conservation, asymmetric perturbations such as multiplication by a phase gradient, $e^{i\eta x}$ with $\eta \ll 1$, cause both 1-bump and 2-bump solutions to oscillate in space around the stationary solution. This is similar to known behavior for 1- and 2-bump gap solitons both in the continuum regime [39] and in discrete models [40] although in the present case the oscillations are more visible. We suspect that these oscillations are largely suppressed by the damping boundary conditions and large

value of $m_1 \sim 6$ for the confining potential that are typically used in the literature [14, 39] in contrast to the case of periodic boundary conditions with the modest value $m_1 = 0.1$ used here. Stable solutions higher up on the snaking branches have dynamics similar to those near the primary bifurcation. Because solutions retain any energy associated with the initial perturbation these stable solitons all execute qualitatively similar dynamics.

Linearly unstable solutions higher up on the snaking branches also all behave in a systematic fashion. Every N-bump solution exists on a stable and unstable branch segment separated by a right fold (Fig. 2). The main difference in the profiles of the solutions on these two segments is the presence of defects on either side as shown in Fig. 3. As can be seen from Fig. 6 an odd parity eigenfunction is always associated to the most unstable eigenvalue. This eigenfunction acts to grow one of the defects and eliminate the other. This causes an N-bump unstable solution to evolve into an oscillatory solution that cycles around another stable snaking state with $N+1$ bumps. This evolution is shown in Fig. 9. The solution oscillates both in position and phase and does so with distinct frequencies, as can clearly be seen by comparing panels (a) and (b). We emphasize here that although the simulation is conducted in a particular rotating frame (fixed m_0) *all* the snaking solutions with different m_0 remain valid solutions in *this* frame although they now rotate in time. Thus, if the solution migrates towards another snaking solution then generically it is expected to rotate as observed. As alluded to above we conjecture that the spatial oscillations would be suppressed or at least damped if the radiation given off were allowed to escape. In this case the stable snaking solution to which the dynamics appear to migrate may become an attractor in time.

When appropriate perturbations are selected the unstable symmetric eigenmode can also be observed. In Fig. 10 the time evolution of a 3-bump snaking solution (point S3 in Fig. 2) is perturbed by the symmetric eigenfunction. The growth of this mode causes the solution to evolve into a breather whose width fluctuates sinusoidally in time. When the solution width expands laterally ($t \sim 200, 500, 700$) the inter-bump height decreases, preserving the L^2 norm. This is best seen in Fig. 10(a) or (c). At $t \sim 800$ this process ends when the more unstable asymmetric mode becomes visible. Because the equation is reflection-symmetric this is likely due to the growth of numerical errors in either the initial condition or the subsequent timesteps. Further time evolution (not pictured) confirms that beyond $t = 800$ both asymmetric and symmetric oscillations occur but the solution still remains localized near a 3-bump snaking state.

Like stable forced snaking solutions, stable solutions in the foliated regime also have simple dynamics. We focus on stable solutions with a phase gradient perturbation. Although there are many qualitatively different types of stable solutions in the foliated regime they all have oscillatory dynamics similar to the forced snaking case. To look at one specific case we consider a 1-lump 2-spike solution from the 1-lump branch with a larger phase gradient perturbation, $\eta = 0.1$. The initial solution, point S4 in Fig. 4, is the last base state pictured in Fig. 7. When the phase gradient is this large the spatial and temporal oscillations are clearly distinguishable (Fig. 11). Furthermore the lumps and spikes appear to oscillate independently with oscillation frequencies that depend on the amplitude and spatial extent of $u(x)$. The lump oscillates in space and rotates in time while the spikes maintain their phase and only oscillate in space. The spatial oscillation frequencies of the two spikes are identical but smaller than that of the central lump.

The dynamics arising from the unstable branches of the foliated snaking states are complicated. We only treat two examples here. Although the FPT made up of clearly separated lumps and spikes are stable, the regime near $m_0 \approx -0.15$ includes a variety of unstable solutions as well. As shown in Fig. 7 unstable solutions may possess a variety of unstable modes but we only focus here on two examples, and only on the most unstable eigenmodes. The first of these, S5 in Fig. 4, is the third base state on the 1-lump branch as pictured in Fig. 7. This state has only one unstable eigenfunction and this eigenfunction is odd. The time simulation in Fig. 12 shows that the solution decays after $t \approx 500$ in a spectacular fashion into three oscillatory pulses and a single traveling pulse. The spatial extent of the oscillatory pulses varies and hearkens to the fact that lumps and spikes vary in amplitude and width with m_0. The oscillatory pulses are deposited in adjacent wells of the potential and oscillate as trapped states.

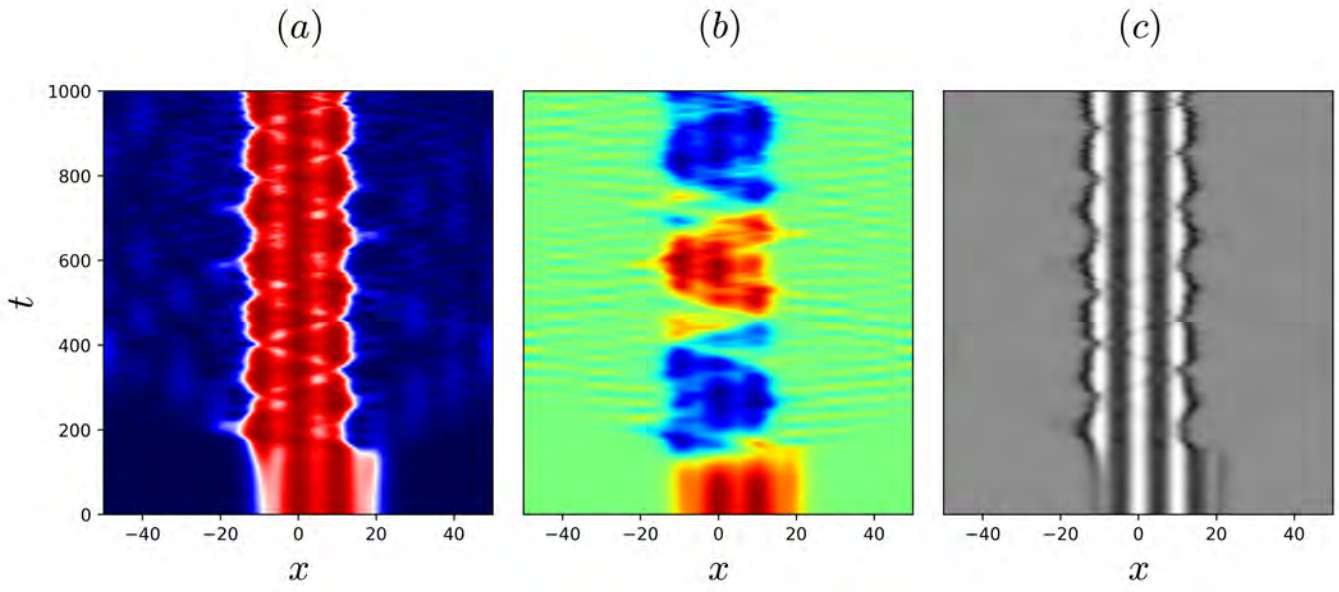

FIG. 9. Time evolution of an unstable 2-bump snaking solution (point S2 in Fig. 2) perturbed by the unstable antisymmetric eigenfunction. The initial condition is the second base state pictured in Fig. 6 on the even branch. The simulation is performed with $m_0 = -\frac{3}{16}$, $\ell = 10$. Plot (a) shows $|u|$, (b) $\Re(u)$ and (c) $E(u)$. The solution decays after $t \approx 180$ into an asymmetric oscillatory state that appears to cycle around a stable three-bump snaking solution. Wave radiation is visible in panel (b).

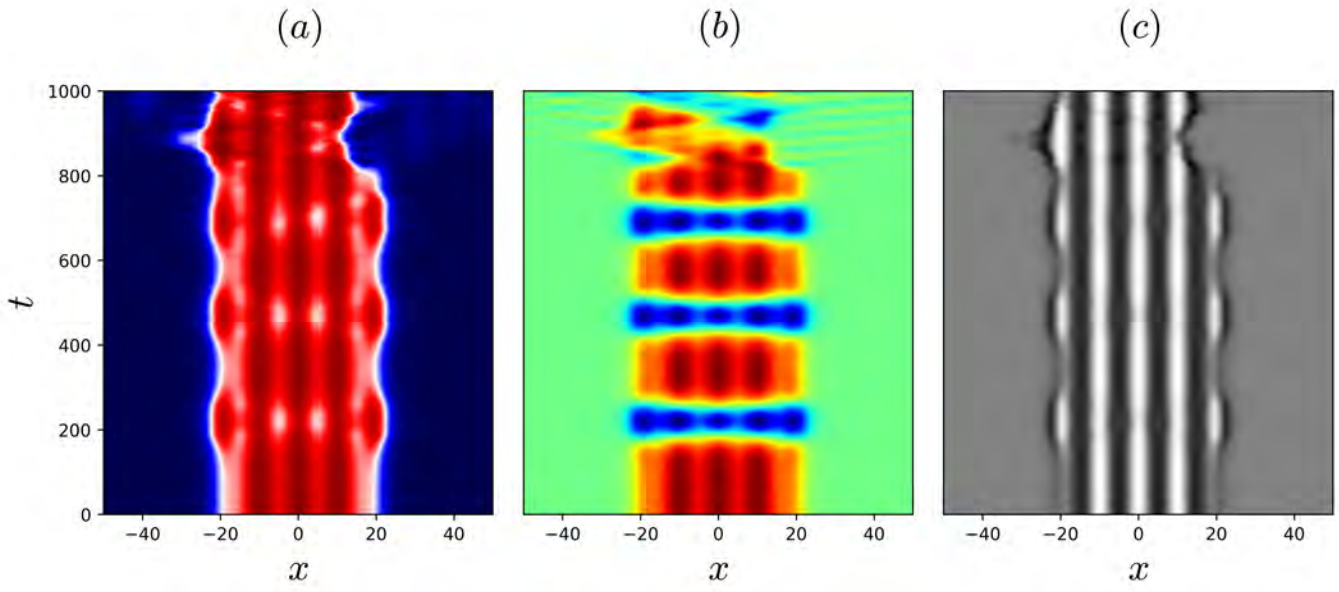

FIG. 10. Time evolution of an unstable 3-bump solution on the odd snaking branch snaking branch (point S3 in Fig. 2) perturbed by the symmetric unstable eigenfunction. The initial condition is the second base state pictured in Fig. 6 on the odd branch. The simulation is performed with $m_0 = -\frac{3}{16}$, $\ell = 10$. Plot (a) shows $|u|$, (b) $\Re(u)$ and (c) $E(u)$. As a consequence of the initial perturbation the solution oscillates symmetrically in space while rotating; at $t \approx 800$ the (more unstable) asymmetric mode becomes apparent. Though not shown here, evolution beyond this point is oscillatory and both symmetric and antisymmetric dynamics occur.

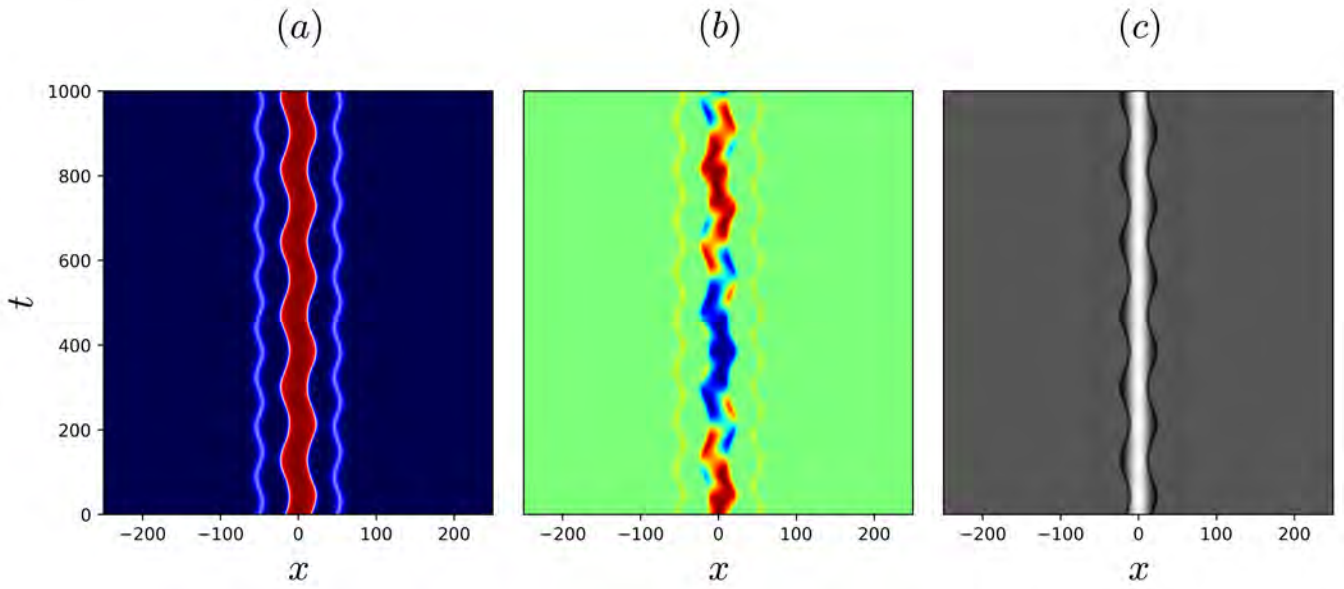

FIG. 11. Time evolution of a stable 1-lump 2-spike solution on the first foliated snaking branch (point S4 in Fig. 4) perturbed by a phase gradient $\eta = 0.1$. The initial condition is the fourth base state pictured in Fig. 7 for the 1-lump foliated branch. The simulation is performed with $m_0 = -0.15$, $\ell = 50$. Plot (a) shows $|u|$, (b) $\Re(u)$ and (c) $E(u)$. As a consequence of the initial phase gradient perturbation the central lump oscillates in space and rotates while the spikes at the sides only oscillate. The frequencies of the oscillations depend on the spatial extent of the lumps/spikes.

The last case of instability we consider is one in which one of the most unstable eigenfunctions is of even parity. The base state, S6 in Fig. 4, is the fourth on the 1-lump branch as pictured in Fig. 7 and the time simulation is shown in Fig. 13. The evolution shows that the state quickly evolves into a breather whose width oscillates regularly in time. We have not investigated even parity instabilities systematically but conjecture that many of them manifest themselves in a similar fashion.

B. Unbinding transitions

The study of traveling solitons in optical latices has a rich history. The specific phenomenon of soliton unbinding and propagation takes the name "mobility" in much of the gap soliton literature. A great deal of work has examined the mobility of solitons in discrete lattices where uniformly traveling solutions do exist; we direct the reader to the review [41] for a comprehensive history. This work includes proofs of existence of traveling solutions [42] and examinations of the effects of phase gradient perturbations on stationary solitons [40]. For example, in [43] the speeds of solitons subject to such a perturbation are computed. To our knowledge less analytical work has been done in the continuum context [44, 45]. A notable exception is Ref. [46] that focuses on a PT-symmetric cubic NLSE with spatially periodic modulation in both linear and nonlinear terms and employs an adaptation of the inverse scattering transform to compute soliton speeds analytically in the shallow potential limit. We are unaware of any similar work on gap solitons in the cubic-quintic NLSE studied in this paper and now turn to examine, both numerically and analytically, the mobility of gap solitons in this context.

Stable stationary gap soliton solutions have a temporal spectrum entirely contained on the imaginary axis and thus oscillate when a small perturbation is added. Since Eq. (1) conserves energy it is natural to parametrize perturbed stationary solitons by their extra energy. When this energy is small the dynamics are determined by the linear spectrum of the stationary solution and are thus oscillatory. For larger energies the dynamics are fully nonlinear. When the energy of the perturbed soliton is sufficiently high it unbinds from the potential allowing the fronts flanking the localized state to propagate. Some of this dynamical behavior is captured by the strongly nonlinear asymptotic analysis contained in Appendix A.

We first turn to asymmetric perturbations. In line with the theory (Appendix A) we consider perturbations with a uniform phase gradient so that the initial condition is $u(x,0) = e^{i\eta x}u_0(x)$ where $u_0(x)$ is a stationary gap soliton solution. As shown in Appendix A the dynamics of the center of mass of such an initial condition follow that of a mathematical pendulum. Specifically, as η is increased from zero the motion transitions from the "libration" regime, in which the soliton's center of mass oscillates with zero average speed, to the "rotation" regime, where the center of mass moves with nonzero average speed. Three snapshots of this transition are shown in Fig. 14. In panel (a) of the figure a 1-lump gap soliton (solution S7 from Fig. 4) with an added initial phase gradient $\eta = 0.1$ executes libration motion. As the initial phase gradient is increased the soliton begins to depin and splits into pulses some of which move with a nonzero average speed (rotation regime) while others remain pinned executing libration. This is shown in panel (b) of Fig. 14 where $\eta = 0.4$. As the leading pulse propagates it deposits "mass" into successive wells of the potential. Because the equation is mass-preserving the leading pulse is drained of mass as this occurs and may itself become trapped (Fig. 15). Further increase in η shifts the motion more solidly into the rotation regime. For large enough η the bulk of the pulse does not split but moves with a single nonzero average speed, Fig. 14(c). Although a small amount of mass appears to escape from the moving pulse the fraction of mass lost is trivial compared to the total. On a periodic domain integration for longer times reveals a stationary state in which the pulse travels at a same constant average speed. The average speeds of the center of mass of these pulses are well predicted by our asymptotics (see below).

The crossover from the libration to the rotation regime is associated with complex behavior, particularly in the long time limit. In the early stages of unbinding solution S7 propagates with a nonzero average speed but still loses mass in the potential. A long time simulation is shown in Fig. 15. The solution propagates while shedding pulses which are trapped by the potential much like occurs for an unstable solution in Fig. 12. Because the domain is periodic the leading pulse eventually collides with the remains of the original state near $t = 700$, giving up most of its mass but allowing a small and faster untrapped pulse to propagate away on the far side. This reconnection is facilitated by the potential and is unlike the true soliton behavior of the unforced NLSE since mass is exchanged between the colliding pulses. A later stage of this dissolution process for a larger perturbation gradient, $\eta = 0.8$, is shown in Fig. 16. Here the bulk of the mass travels with a nonzero average speed. Fracturing of the leading pulse leads to smaller pulses that are slower but still untrapped Only a small amount of mass is trapped in the wells of the potential. As time progresses splitting of the pulses continues until masses traveling at a range of average speeds are present. Of particular interest are the small amplitude quasistationary structures deposited by the drifting pulse; these represent lost mass trapped in different wells of the potential. We have not investigated this behavior for arbitrarily large domains but here, in a finite domain, the solution appears to reach a pseudo-steady state. We conjecture that on an infinite domain the initial pulse or soliton disintegrates in a similar fashion, and eventually ceases to exist as an identifiable structure. As η increases further the pulses travel at larger and larger average speeds and appear to execute fewer oscillations. These oscillations are never

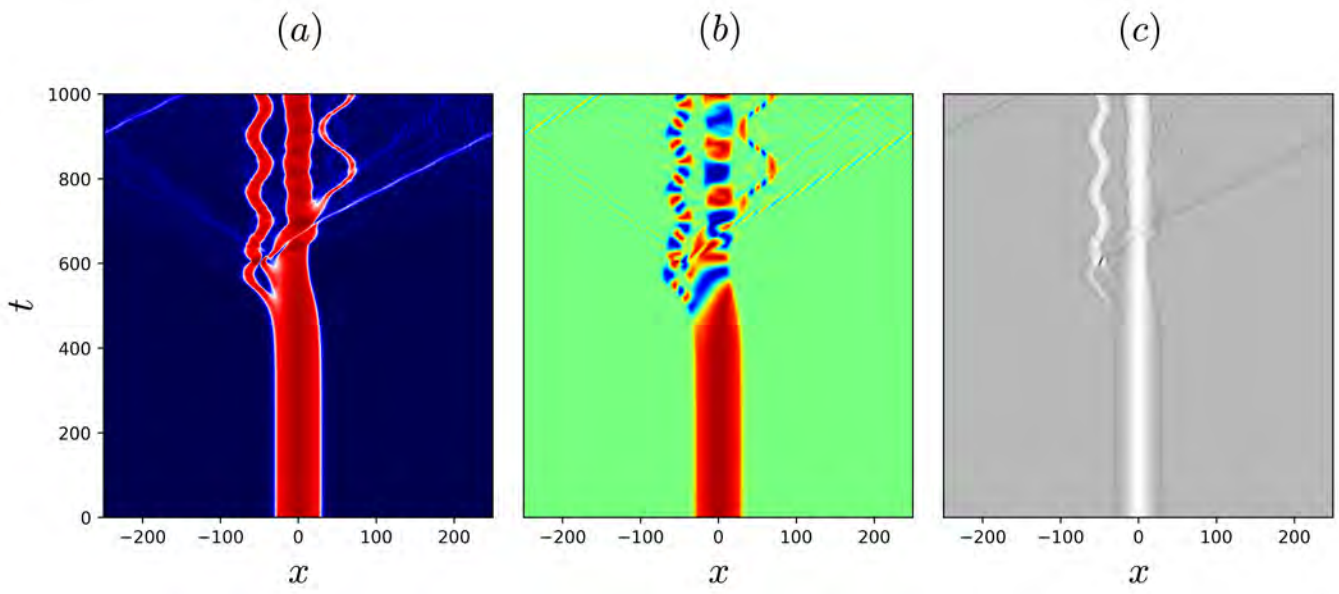

FIG. 12. Time evolution of a 1-lump unstable solution on the first foliated snaking branch (point S5 in Fig. 4) perturbed by an unstable antisymmetric eigenfunction. The initial condition is the third base state pictured in Fig. 7 on the 1-lump foliated branch. The simulation is performed with $m_0 = -0.1$, $\ell = 50$. Plot (a) shows $|u|$, (b) $\Re(u)$ and (c) $E(u)$. The solution decays after $t \approx 500$ into four distinct states. Three of these oscillate in space and phase and appear to cycle around a variety of 1-pulse solutions. The oscillation frequencies depend on the height and spatial extent of the pulses. A remaining pulse is shed with a definite average speed to the right and in an infinite domain we expect this "radiation" to continue propagating to infinity.

eliminated, however, since states traveling at constant speed cannot exist in equations like Eq. (1) when m_1 is nonzero, cf. [47].

We next examine the effect of a symmetric perturbation on the unbinding transition. In order to study symmetric modes we consider a phase perturbation of a stationary gap soliton that is symmetric with respect to the soliton's center of mass. Specifically, we take initial conditions of the form $u(x,0) = e^{i\rho(x-\alpha)^2}u_0(x)$, where $x = \alpha$ represents the location of the soliton's center of mass.

Because of the mass-conserving property of Eq. (1) symmetric perturbations of sufficient amplitude cause a qualitatively different transition from antisymmetric ones. As in the antisymmetric case the local phase gradient at the position of the fronts flanking the localized state determines the direction of the front motion. In the antisymmetric case the phase gradient at both fronts is identical and both fronts move in the same direction with the same speed, regardless of whether the motion is a libration or a rotation. The main qualitative difference in the symmetric case is that the sign of the phase gradient is now opposite at the two fronts. As a result for small ρ each front moves with the same speed but in *opposite* directions generating a state that is a symmetric analog of libration, i.e., a breathing state, as shown in Fig. 17(a) where $\rho = 0.01$. As can be discerned from the coloring of the plot the amplitude of the pulse grows when its width decreases and vice versa. Thus the dynamics conserve the soliton mass. When ρ is increased to a sufficient extent the fronts acquire a nonzero mean speed and propagate outward away from the center of the structure, Fig. 17(b). This causes a competition between the growth in width of the pulse and decrease in its amplitude. For $\rho = 0.02$, panel (b), the fronts detach from the central structure in the form of two traveling pulses, and leave a librating or breathing mode at the center. For even larger gradients, $\rho = 0.1$ in panel (c), the soliton expands yet more rapidly although a breathing structure in the center remains. We have found a qualitatively similar sequence of transitions for other symmetric perturbations, such as $e^{i\rho|x-\alpha|}u_0(x)$, and conjecture it to be generic.

Perturbations that involve a combination of symmetric and asymmetric parts exhibit similar "two regime" dynamics. We do not perform a complete analysis of the general case, $e^{i\eta(x-\alpha)+i\rho(x-\alpha)^2}u_0(x)$, but provide two examples in Figs. 18(a) and (b). In Fig. 18(a) we set $\eta = 0.1$, $\rho = 0.01$ and show that the gap soliton falls into a libration regime in which both symmetric and antisymmetric oscillations of different periods occur. For larger η and ρ [$\eta = 0.2$, $\rho = 0.02$, Fig. 18(b)] the soliton undergoes an asymmetric unbinding in which a significant fraction of the mass escapes in a series of pulses traveling to the right, in addition to smaller amplitude radiation that is present already in panel (a), leaving a librating mode at the origin. The process of unbinding is evidently complex and we do not attempt to analyze it further. In principle one could predict thresholds in the (η, ρ) parameter space for the unbinding transition but we leave this type of analysis to future work.

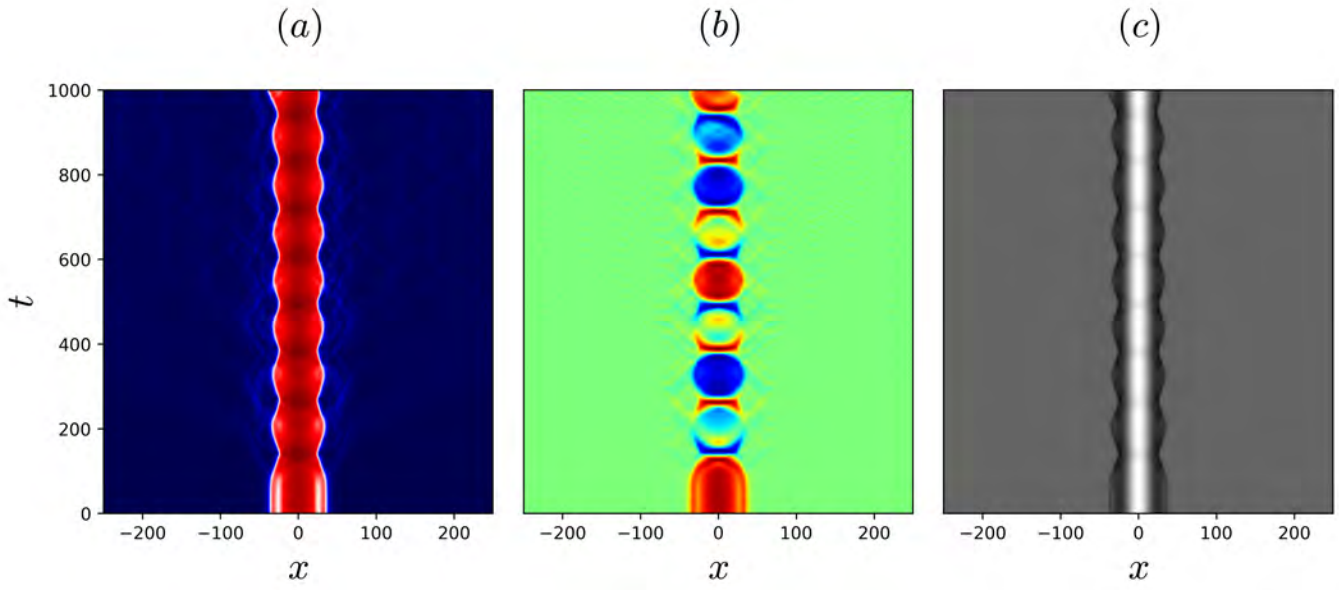

FIG. 13. Time evolution of a 1-lump unstable solution on the first foliated snaking branch (point S6 in Fig. 4) perturbed by the symmetric unstable eigenfunction. The initial condition is the fourth base state pictured in Fig. 7 on the 1-lump foliated branch. The simulation is performed with $m_0 = -0.15$, $\ell = 50$. Plot (a) shows $|u|$, (b) $\Re(u)$ and (c) $E(u)$. After $t \approx 100$ the solution decays into a breather that maintains its parity in space but oscillates in space, phase and amplitude.

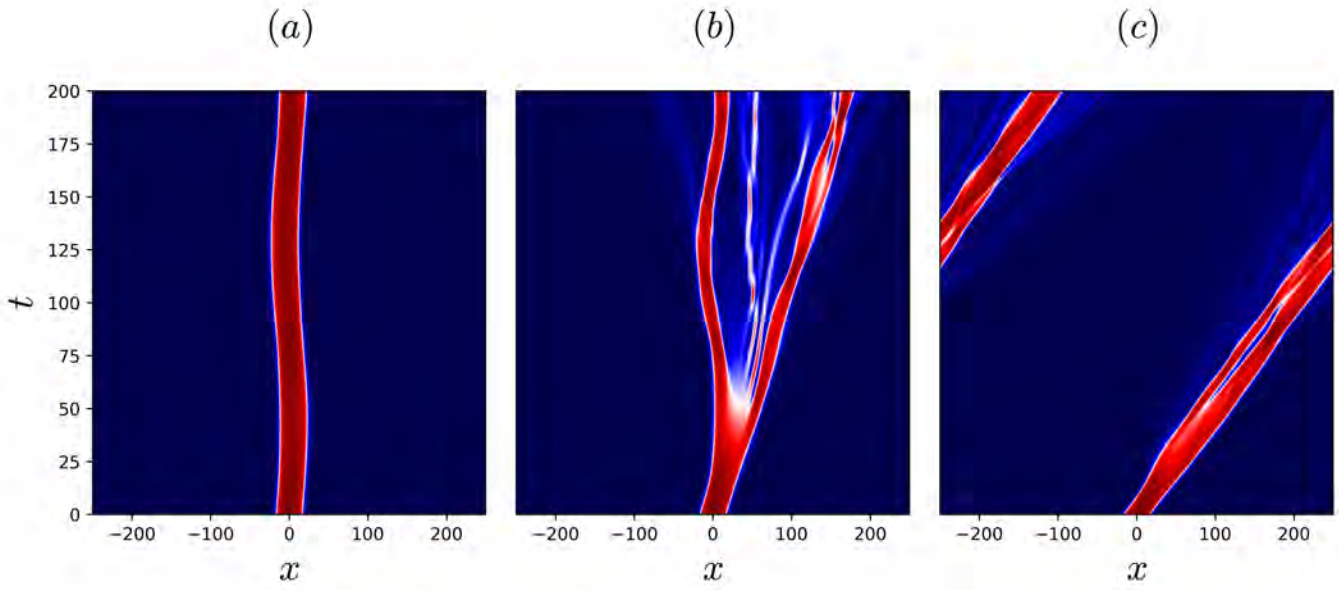

FIG. 14. Time evolution of a stable 1-lump solution on the first foliated snaking branch (point S7 in Fig. 4) with a phase gradient perturbation of magnitude (a) $\eta = 0.1$, (b) $\eta = 0.4$ and (c) $\eta = 1$ shown in terms of a space-time plot of $|u(x,t)|$. The simulation is performed with $m_0 = -0.15$, $\ell = 50$. For small η (a) libration occurs. As η is increased the solution begins to unbind (b) and when η is sufficiently large the solution travels with nonzero average speed (c).

C. Analysis of coherent states

In this section we project the time evolution dynamics of the previous sections onto the two degrees of freedom described by the theory in Appendix A. This theory is designed to capture the dynamics of the center of mass of a pulse-like solution, for which we derive an ODE, and is therefore applicable to dynamics governed by spatially asymmetric modes. Concretely, the theory applies to scenarios such as those portrayed in Figs. 9, and 11 but not those in Figs. 10 or 13. The theory also applies in situations where the center of mass has a nonzero aver-

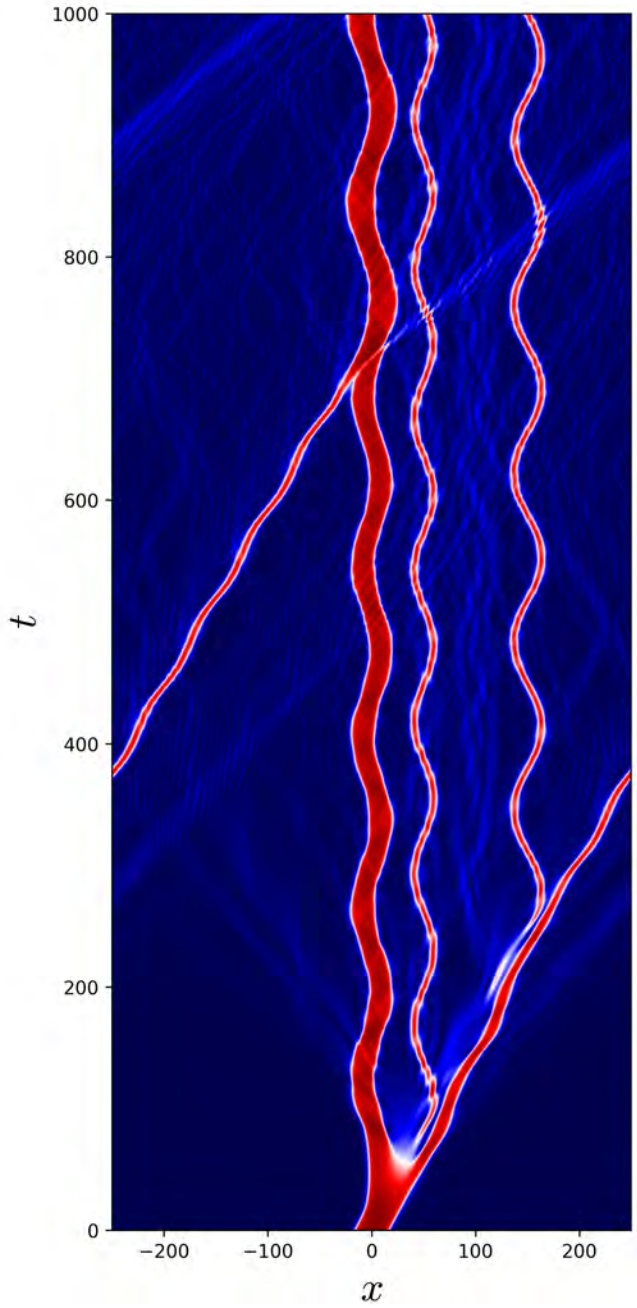

FIG. 15. Long time evolution of a stable 1-lump solution on the first foliated snaking branch (point S7 in Fig. 4) with a phase gradient perturbation of magnitude $\eta = 0.3$ shown in terms of a space-time plot of $|u(x,t)|$. The simulation is performed with $m_0 = -0.15$, $\ell = 50$. The simulation shows that initially the pulse propagates with the theoretically predicted velocity but soon breaks up at $t \approx 50$ into an oscillating structure and a propagating pulse which subsequently sheds mass into the wells of the potential depositing a sequence of trapped pulses. Because the domain is periodic a collision between the remaining traveling pulse and the original pulse occurs near $t \approx 700$ resulting in the reabsorption of most of its mass by the original pulse and diffraction of the traveling pulse that remains.

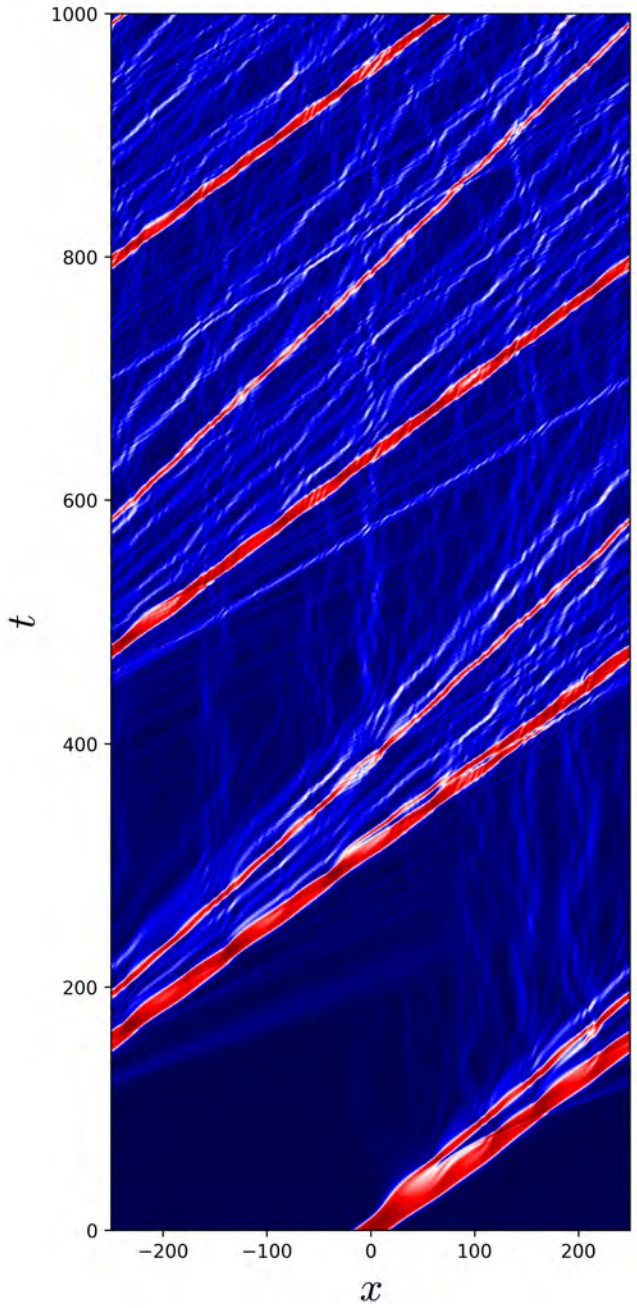

FIG. 16. Long time evolution of a stable 1-lump solution on the first foliated snaking branch (point S7 in Fig. 4) with a phase gradient perturbation of magnitude $\eta = 0.8$ shown in terms of a space-time plot of $|u(x,t)|$. The simulation is performed with $m_0 = -0.15$, $\ell = 50$. The simulation shows that even at late times the solution continues to propagate and shed mass into the wells of the potential. Because the domain is periodic a type of pseudo-steady state is achieved at very long times in which the solution mass disperses into components propagating at a range of speeds.

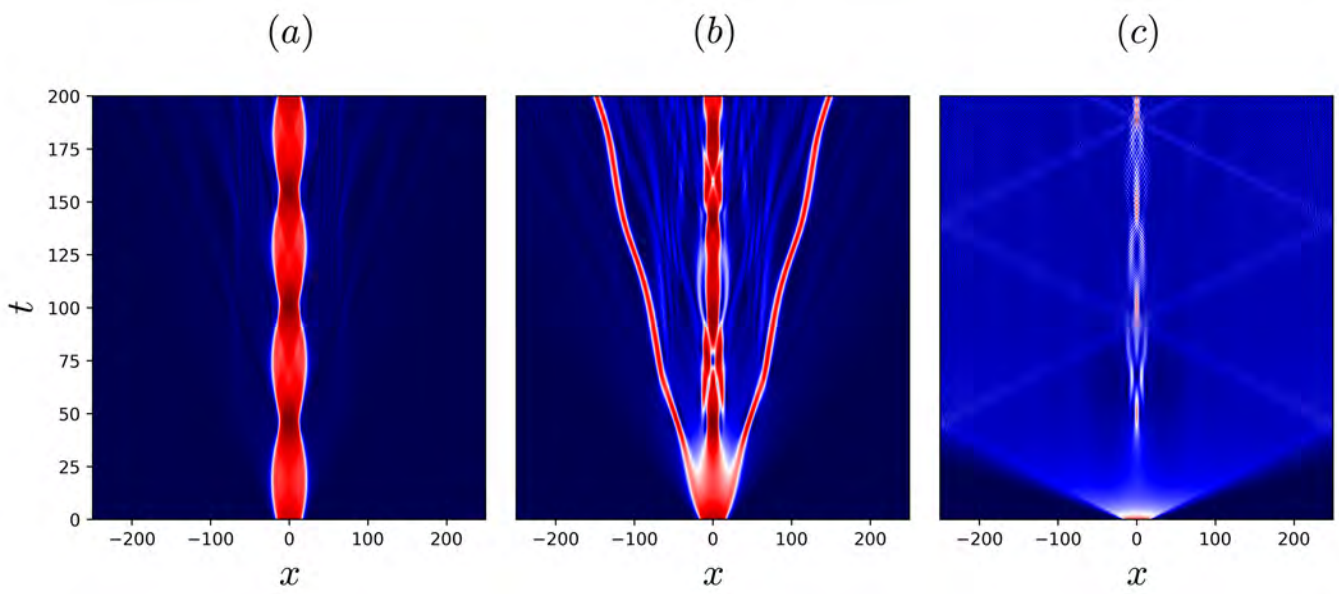

FIG. 17. Time evolution of a stable 1-lump solution on the first foliated snaking branch (point S7 in Fig. 4) with a symmetric phase gradient perturbation of magnitude (a) $\rho = 0.01$, (b) $\rho = 0.02$, (c) $\rho = 0.1$ shown in terms of a space-time plot of $|u(x,t)|$. The simulation is performed with $m_0 = -0.15$, $\ell = 50$. For small ρ (panel (a)) breathing motion occurs. As ρ is increased the solution begins to unbind symmetrically and the fronts bounding the pulse propagate in opposite directions with identical speeds (panels (b) and (c)).

age speed as in the case of the first unbinding transition (Fig. 14).

We divide this section as follows. We first discuss the application of our theory in the libration regime for a pulse with a phase gradient perturbation. In this case the PDE initial condition can be mapped directly to an initial condition for the ODE. Next we describe the evolution shown in Fig. 9 in which an unstable solution evolves into an oscillatory coherent state. In this case we do not know the initial conditions for the ODE. Finally, we discuss the application of the theory in the rotation regime and compute the average speed of a traveling pulse.

As a first application of the theory in Appendix A we turn to the evolution of the single pulse solution S7 with a phase gradient perturbation $\eta = 0.1$. This is the same simulation as that shown in Fig. 14(a) but we integrate the solution until $t = 3000$. Although the full time evolution plot is omitted here the dynamics are nearly identical to those of the central pulse in Fig. 11. The Ansatz for the solution that is used in our theory is

$$A(x,t) = e^{i\int \omega(t)dt + i\frac{\dot{\alpha}(t)}{2}(x-\alpha)} v(x,t)$$

where v is a near-stationary pulse and α is its time-dependent center of mass (see Appendix A for more details). At every time step we compute the center of mass, $x = \alpha(t)$, of the solution using Eq. (B3) and extract the phase $\int \omega\, dt$ from the nearest point on the mesh to $x = \alpha$. We use the result to define a phase-like quantity $\theta(t)$ such that $\int \omega\, dt = \omega_0 t + \theta(t)$ and compute it by fitting a linear regression to $\int \omega\, dt$ and subtracting $\omega_0 t$. The time series for α and θ are easiest to understand in Fourier space and are shown in Fig. 19(a) and (b). These signals can be messy and difficult to differentiate with respect to time which is required to compare the numerical results with the ODE description. To regularize them we set to zero all Fourier amplitudes corresponding modes with wavenumber outside the boundary of the figure. After regularization the frequency ω is reconstructed by differentiating θ in Fourier space and adding back the slope of the trend in real space. Finally, a snapshot of the solution amplitude is shown at a fixed time in Fig. 19(c) in order to map the pulse width onto the theory. Here we show the theoretically predicted pulse width L (dashed black line) according Appendix A along with an empirically determined width (grey line). These lines indicate the locations of the fronts bounding the structure at each instant in time.

We evaluate the accuracy of the ODE description of the PDE dynamics (Eqs. (A3)-(A4)) using three distinct projections as depicted in Fig. 20. The first of these, (a) in the figure, uses the energy of the solution (Eq. (6)). We plot the PDE energy, $\mathcal{E}$, using a dashed black line which is conserved along with the energy in the Ansatz used in the theory, Eq. (A1). After performing the energy integral with Eq. (A1), the *Ansatz energy* becomes a function of α and $\dot{\alpha}$ ($\mathcal{E} = f(\alpha, \dot{\alpha})$) which we evaluate using the measured signal. Because of inaccuracies arising from the numerical differentiation of the signal near the boundary of the time domain we suppress the plotted signal near the boundary both here and in subsequent plots in this section. A red line denotes the average of the Ansatz

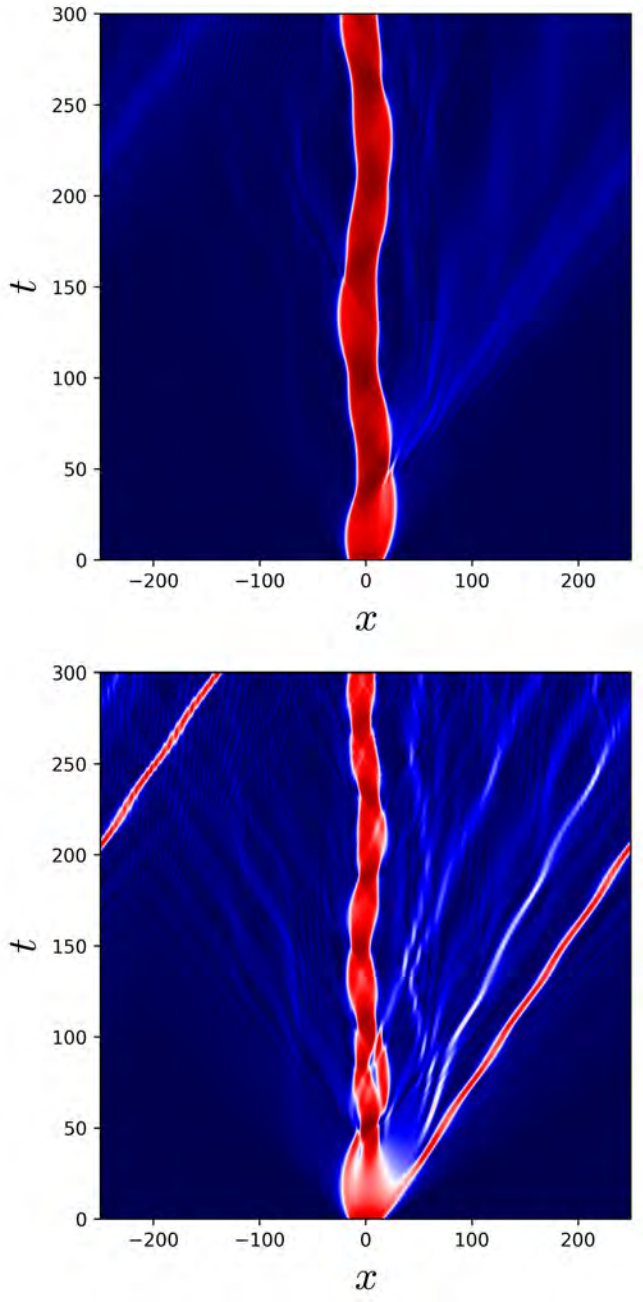

FIG. 18. Time evolution of a stable 1-lump solution on the first foliated snaking branch (point S7 in Fig. 4) with phase perturbation (a) $(\eta, \rho) = (0.1, 0.01)$ and (b) $(\eta, \rho) = (0.2, 0.02)$ shown in terms of a space-time plot of $|u(x,t)|$. The simulation is performed with $m_0 = -0.15$, $\ell = 50$.

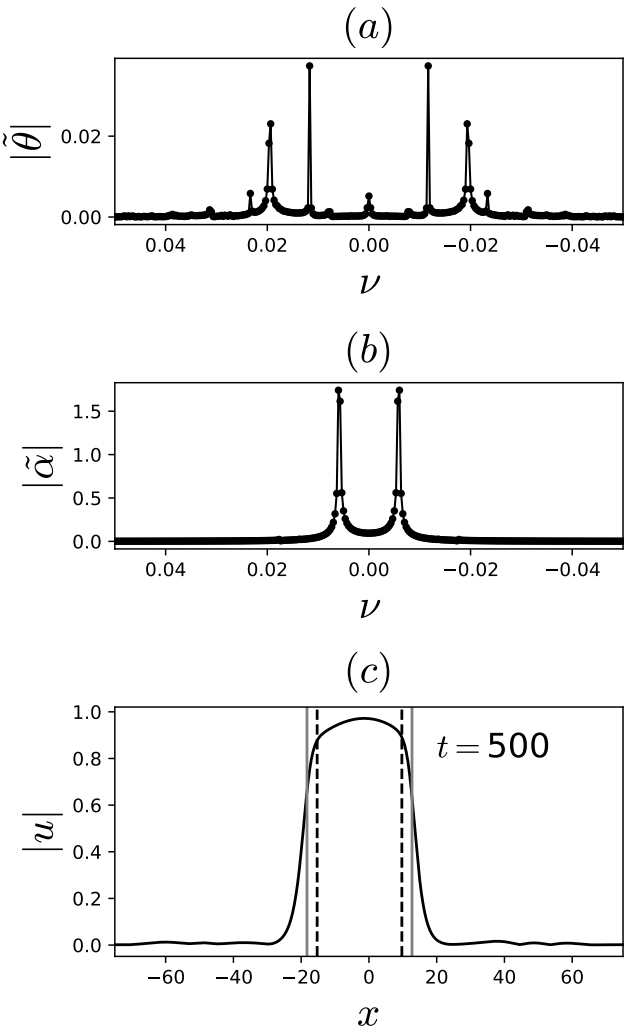

FIG. 19. Amplitude of a discrete Fourier transform of the time series for (a) $\theta(t)$ and (b) $\alpha(t)$ as a function of the Fourier space wave number ν for the time evolution of solution S7 with $\eta = 0.1$. All Fourier amplitudes corresponding to frequencies beyond the domain size are set to 0. (c) $|u(x, 500)|$ on the interval $[-100, 100]$ along with lines denoting the positions of the fronts. Each pair of lines is placed symmetrically with respect to $\alpha(500)$: width $L = 25$ (black dashed) and width $L = 31$ (grey).

energy. Though the Ansatz energy fluctuates in time its average represents approximately $\sim 84\%$ of the total energy. This mismatch is likely a consequence of the fact that the Ansatz is a low order approximation allowing energy loss in the form of radiation (which is not in our Ansatz), and that the sampling of $\alpha(t)$ is insufficiently precise. This is potentially the cause of the very slight drift in Ansatz energy (Fig. 20(a)) seen over the sampling interval.

The second projection, Fig. 20(b), is onto the phase space of Eq. (A4). We plot the trajectory in the space $(\beta, \dot{\alpha})$ where $\beta = \sqrt{\frac{2\lambda\ell}{\pi}} \sin\left(\frac{\pi L}{\ell}\right) \sin\left(\frac{\pi\alpha}{\ell}\right)$. In these variables true trajectories of the ODE are circles. By inspecting Eq. (A1) it is evident that an initial phase gradient perturbation η corresponds to an initial value $\dot{\alpha}(0) = 2\eta$ for the ODE. The ODE trajectory corresponding to this initial condition is shown as a red circle. In order to plot the sampled dynamics the pulse width, L, must be specified. The theory predicts that $L = 25$ (shown in black)

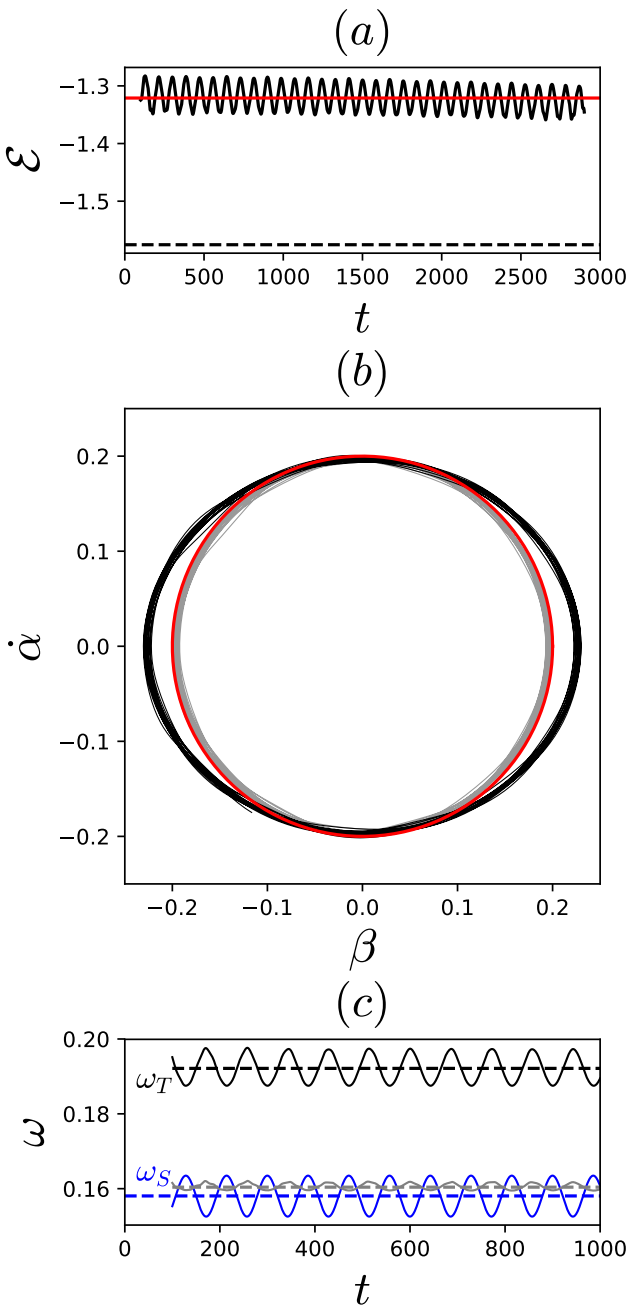

FIG. 20. ODE projections for dynamics of solution S7 with $\eta = 0.1$. (a) The PDE energy $\mathcal{E}$ (Eq. (6)) as a function of time (black dashed) along with the instantaneous energy $\mathcal{E}(t)$ from the Ansatz (A1) (black solid) and its mean (red). (b) $\alpha(t)$ in the phase space of Eq. (A4) where $\beta = \sqrt{\frac{2\lambda\ell}{\pi}}\sin\left(\frac{\pi L}{\ell}\right)\sin\left(\frac{\pi\alpha}{\ell}\right)$. Trajectories of the sampled signal are plotted for the cases $L = 25$ (black) and $L = 31$ (grey) along with the analytical trajectory for the initial condition $\dot{\alpha}(0) = 0.2$ (red). (c) The sampled signal ω_S as a function of time (blue) along with ω_T for the cases $L = 25$ (black) and $L = 31$ (grey). The means of the signals are shown with a dashed line. To make the periods distinguishable the signals are plotted up to $t = 1000$ though the time evolution is carried out to $t = 3000$.

but we also plot an empirically chosen width $L = 31$ in grey (see Fig. 19(c)). Although the theoretical prediction is not far off, the grey curve is in near perfect alignment while the black curve is not. We suspect that this has to do with the extent to which the Ansatz can model lump states at *lowest* order and conjecture that a higher order asymptotic calculation would lead to an improved prediction of the location of the two fronts.

The last projection onto the ODE, Fig. 20(c), examines the prediction for the frequency ω. Theory predicts that $\omega = \frac{3}{16} + \epsilon\,\omega_2(t) \equiv \omega_T$ which we plot for $L = 25$ (black) and $L = 31$ (grey) along with the sampled signal $\omega \equiv \omega_S$ (blue). The averages of the signals are plotted with dashed lines. The figure shows that despite the fact that the signals are not perfectly periodic the dominant period is the same for all three and ω_S is exactly out of phase with the other two. When we use the theoretically predicted width $L = 25$, we find that the amplitudes of the oscillations inω_T and ω_S are in good agreement although their means differ. However, with the empirically determined width $L = 31$ the means also fall into agreement. It is worth noting here that because the evolution of the PDE solution behaves as $e^{i\int\omega\,dt}$ the mean of ω provides the dominant contribution to the oscillations observed in the $\Re(u)$ plots earlier in this section.

Next we turn to the evolution in Fig. 9. Because there is an initial transient during which the initial condition destabilizes before entering a coherent state we measure the signals α and ω only after $t \sim 300$. The signals are much noisier in this case although the same double peak signal is present for α (not pictured). In this case we have chosen not to set an empirical pulse width and use the analytical prediction $L = 25$. The ODE projections are shown in Fig. 21. Here the Ansatz energy, panel (a), appears to be much noisier than in the previous case. This is likely due both to the relative increase in radiation which is visible in Fig. 9 and also to the fact that the PDE solution does not map directly to a single ODE trajectory. This is because the projection of the PDE dynamics provides a 1D picture of the dynamics in the ODE phase space. Unlike the case of a phase gradient perturbation, which maps to a unique ODE trajectory, arbitrary perturbations of the PDE solutions can lead to energy transfer between different PDE modes potentially resulting in the evolution of the ODE energy when projected down to the ODE phase space even though the ODE conserves energy.

Despite the noise, the average energy is again close to the total PDE energy and we therefore argue that the model captures a significant portion of the dynamics. Using the mean Ansatz energy an initial value for $\dot{\alpha}$ can be constructed by setting $\alpha = 0$. The ODE trajectory corresponding to this energy level is plotted in Fig. 21(b) in red along with the sampled trajectory for α in black. The solution can be seen to oscillate near the red line although occasionally it makes deviations. Since the PDE dynamics occur in a nominally infinite-dimensional phase space we cannot hope to capture all the details using a 1D

model. However, the agreement that we see in panel (b) of the figure suggests that despite this fact our 1D theory does indeed capture a large portion of the dynamics even though energy contained in other PDE modes does cause deviations from the ODE phase space trajectory.

Panel (c) of Fig. 21 shows the behavior and prediction of the phase. As is obvious from Fig. 9(b) the phase behavior in this simulation is complicated and sampling ω is somewhat messy. Despite regularizing the signal the sampled phase (blue curve) likely has an exaggerated amplitude although the mean should be accurate. We find that the theoretical prediction with $L = 25$ agrees well with this mean (black line) and this is so for the oscillation period as well. The oscillations do not, however, agree in amplitude.

To close this section we look at the theoretical predictions in Appendix A for the rotation regime. Specifically we return to the evolution of solution S7 with a large phase gradient perturbation (Fig. 14(b) and (c)). Our theory predicts that for sufficiently large phase gradients the center of mass of the solution will begin to propagate with nonzero mean speed. This speed can be computed analytically as done in Appendix A. In Fig. 22 we show this analytical prediction (black) along with the numerically measured speeds for increasing initial phase gradient η (blue points). The simulations are carried out by timestepping the solution to $t = 100$ and tracking the center of mass $x = \alpha(t)$. A linear regression is fit to the trajectory in order to measure the speed. For lower values of η, nearer the transition from the libration regime, the speed measurement is less accurate. By $\eta = 0.8$ the measured and predicted speeds are in near perfect agreement. Although not shown here we have verified that Eq. (A3) also becomes increasingly accurate as η moves farther into the rotation regime.

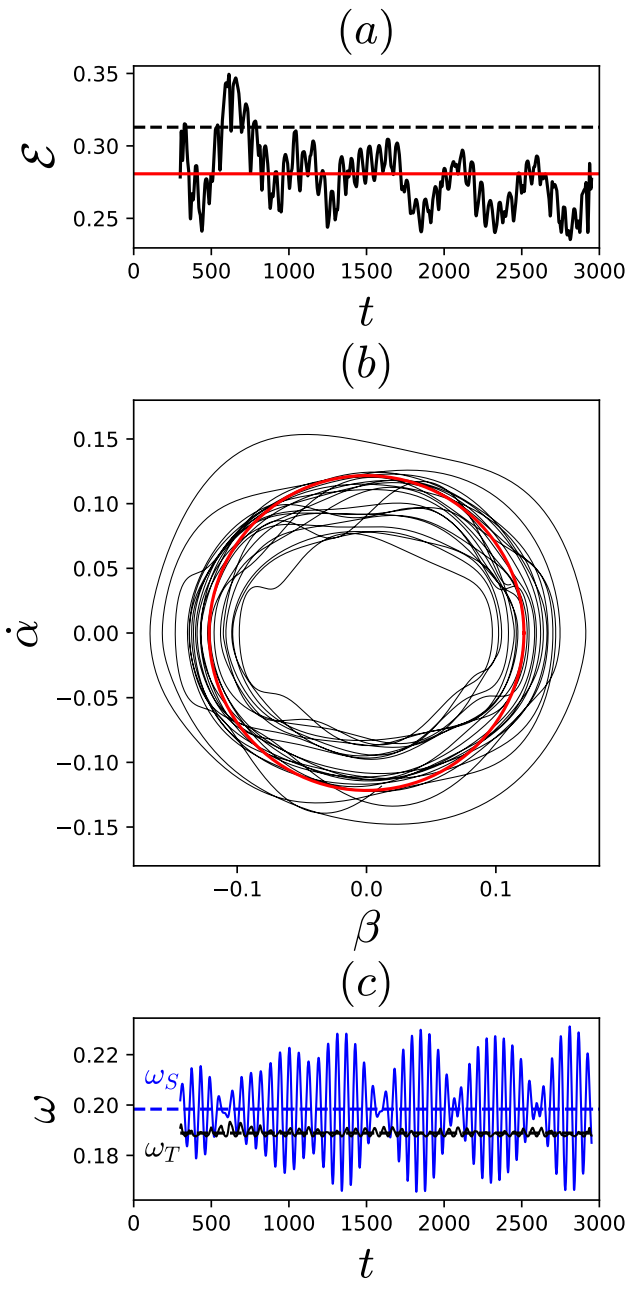

FIG. 21. ODE projections for dynamics of Fig. 9. (a) The PDE energy $\mathcal{E}$ (Eq. (6)) as a function of time (black dashed) along with the instantaneous energy $\mathcal{E}(t)$ from the Ansatz (A1) (black solid) and its mean (red). (b) $\alpha(t)$ in the phase space of Eq. (A4) where $\beta = \sqrt{\frac{2\lambda\ell}{\pi}} \sin\left(\frac{\pi L}{\ell}\right) \sin\left(\frac{\pi\alpha}{\ell}\right)$, with the black line showing the PDE trajectory for the sampled signal with $L = 25$ and the red line the trajectory from Eq. (A4) with initial condition determined by the mean Ansatz energy. (c) The sampled signal ω_S as a function of time (blue) along with ω_T for the case $L = 25$ (black). The means of the signals are shown with a dashed line.

V. DISCUSSION

Owing to the enormous body of work on gap solitons we begin the discussion by emphasizing the key new results in this work.

- We show that the lengthscale of the periodic potential, ℓ, can greatly affect the bifurcation structure of the solutions that are present in the semi-infinite gap. We report *new* gap solitons exhibiting foliated snaking along with their bifurcation structure and stability. Specifically we show that solutions are either "multipulse solitons" exhibiting classical snaking or "soliton complexes" exhibiting foliated snaking, depending on ℓ and m_1.

- We demonstrate that gap solitons depin in a systematic fashion when perturbed by asymmetric and symmetric phase gradients.

- We provide a strongly nonlinear theory to describe the dynamics of gap solitons subject to a phase gra-

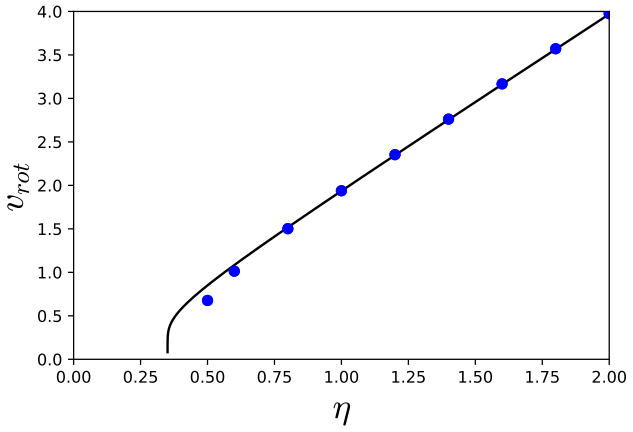

FIG. 22. Average speed v_{rot} of the center of mass of solution S7 as a function of η, the phase gradient of the applied perturbation. The theoretical prediction given by Eq. (B 3) is shown in black while the empirical speed obtained from the simulation results is shown in blue.

dient perturbation. This theory accurately predicts the speeds of rapidly propagating solitons.

The impact of the lengthscale of the potential, ℓ, is derived from its relation to the spatial decay rate of fronts in the unforced equation. When $m_1 = 0$ Eq. (2) has a unique lengthscale, λ, determined by the decay rate of fronts that connect $u = 0$ to $u = \frac{\sqrt{3}}{2}$. These fronts have a spatial decay rate equal to the spatial eigenvalue of the linearization around $u = 0$. These fronts are used in our asymptotic analysis in Appendix A. This lengthscale persists when $m_1 > 0$ and its value relative to the imposed lengthscale of the potential determines the bifurcation structure of localized solutions. In the limit $\ell \ll \lambda$ the fronts span multiple periods of the potential and classical snaking results. In the gap soliton literature these states are frequently referred to as multipulse solitons. In the opposite limit, $\ell \gg \lambda$, a pair of fronts fits inside each period of the potential thus supporting a single pulse at every cosine maximum. This is the foliated snaking regime and the resulting states are frequently known in the literature as soliton complexes. We show that the choices $\ell = 10$ and $\ell = 50$ are able to capture these two distinct regimes although m_1 must be sufficiently large to establish foliated snaking. In sufficiently shallow potentials we conjecture that classical snaking occurs always.

Turning to dynamics we show that gap solitons depin from the potential under sufficiently large phase gradient perturbations and capture this behavior with a strongly nonlinear theory. Through our theory of soliton depinning we were able to identify the two broad dynamical regimes (libration and rotation) that result from phase gradient perturbations. Specifically, the theory shows that the dynamics of the center of mass behaves like a pendulum. By extrapolating from the numerical simulations of symmetric perturbations we can conjecture that each front bounding the localized states has this pendulum-type behavior. Of particular interest is our observation of soliton fission, in which a depinned soliton radiates energy and breaks up into less energetic components that can then become trapped again.

The main natural extension of this work is to higher dimensions, cf. [13]. A significant literature already exists on localized snaking solutions in discrete and continuous models in two and three dimensions. To our knowledge the effects of the potential lengthscale have not been studied in these contexts and foliated snaking is likely to play an important role.

Further extension of this work to study of the effects of ℓ on gap solitons in higher gaps is also envisaged. These gap solitons are quite different than those in the semi-infinite gap studied here since there is no stable stationary front when $m_1 = 0$ out of which they can be constructed. Of course, the possibility that classical and foliated snaking may be differentiated in experiments in photonic systems is also exciting. Some work along these lines has been initiated in dissipative systems that also exhibit forced snaking [48] but we are not aware of any such work in optical systems.

VI. ACKNOWLEDGMENTS

This work was supported by the National Science Foundation under grant DMS-1613132.

Appendix A: Asymptotics for oscillations

We perform an asymptotic analysis in the limit $0 < m_1 \ll 1$ in order to extract equations of motion for localized structures. It is known that Eq. (2) has an exact front solution when $m_1 = 0$ for appropriate values of m_0. This front solution is translation-invariant and its reflection ($x \to -x$) is also a solution. Therefore the basic idea behind our method is to use a pair of these fronts to form a pulse solution. In the $m_1 = 0$ case such a pulse is not a stable solution but in the presence of the periodic potential the fronts are able to pin thereby stabilizing the structure. This technique has been used by a number of previous authors in order to study front dynamics and pinned states [49, 50].

Our Ansatz for a time-dependent solution to Eq. (1) is as follows,

$$\begin{aligned} A(x,t) &= e^{i\int \omega(t)dt + i\frac{\dot{\alpha}(t)}{2}(x-\alpha)} v(x,t) \\ v(x,t) &= aB\left(-\left[x - x_L\right]\right) B\left(x - x_R\right) + W(x,t) \\ x_L &= \alpha - \frac{L}{2} \\ x_R &= \alpha + \frac{L}{2}. \end{aligned} \tag{A1}$$

Here a is a real constant and $aB(x)$ is the front solution to Eq. (2) when $m_1 = 0$; the correction W is assumed

to be small. The two real-valued functions α and ω are selected in order that this Ansatz solve Eq. (1). The two fronts that bound the localized structure are located at $x = x_L$ and $x = x_R$ with $x = \alpha(t)$ representing the center of mass motion (i.e., the antisymmetric dynamics of the pulse). Thus L is the (fixed) pulse width.

In order to ensure that the Ansatz (A1) satisfies Eq. (1) at leading order the two fronts must be placed sufficiently far apart. Although $u(x,t) = aB(x)$ is an exact solution to Eq. (1) when $m_1 = 0$, $\tilde{u}(x) = aB(x)B(-x+L)$ is not. On the other hand, there does exist an *exact* pulse solution that is exponentially close to $\tilde{u}$. The use of a pair of fronts rather than an exact pulse solution simplifies both the calculations that follow and their interpretation. The error incurred is exponentially small in L and we therefore assume that L is sufficiently large that it is negligible in what follows.

1. Asymptotic procedure

We begin the procedure by defining the scaling of the terms in Eq. (A1). The dynamics that we capture occur on a slow time τ, $\tau = \epsilon t$, where $\epsilon \ll 1$ is a suitably defined small parameter. We work in the center of mass frame, $z = x - \alpha$, and adopt the following scaling for the instantaneous frequency and forcing:

$$\omega(\tau) = \frac{\omega_0}{\epsilon} + \omega_1(\tau) + \epsilon\omega_2(\tau)$$
$$m_1 = \epsilon^2\mu.$$

The resulting equation for $v(z,\tau)$ is

$$0 = i\epsilon v_\tau + \epsilon^2\left[\left(\frac{\dot{\alpha}}{2}\right)^2 - \frac{\ddot{\alpha}}{2}z + \mu\cos\left(\frac{2\pi(z+\alpha)}{\ell}\right)\right]v - (\omega_0 + \epsilon\omega_1 + \epsilon^2\omega_2)v + v_{zz} + |v|^2v - |v|^4v$$

and we expand v as follows:

$$v(x,t) = W_0(z) + \epsilon W_1(z,\tau) + \epsilon^2 W_2(z,\tau).$$

The lowest order equation is

$$0 = W_{0zz} - \left(\omega_0 - |W_0|^2 + |W_0|^4\right)W_0. \qquad \text{(A2)}$$

It follows that if $\omega_0 = \frac{3}{16}$ then Eq. (A2) has the front solution

$$W_0(z) = \frac{\sqrt{3}}{2}\sqrt{\frac{1}{1+e^{\frac{\sqrt{3}}{2}z}}} \equiv \frac{\sqrt{3}}{2}B(z).$$

Using the fact that $\frac{\sqrt{3}}{2}B(-z)$ is also a solution, two of these fronts can be patched together to form the Ansatz as described above. Specifically we take $W_0(z) = \frac{\sqrt{3}}{2}B\left(-\left[z+\frac{L}{2}\right]\right)B\left(z-\frac{L}{2}\right) \equiv \frac{\sqrt{3}}{2}B_1(-z)B_2(z)$. This solution is not exact but results in only a small error if L is large compared to the spatial decay rate of the front, $\frac{2}{\sqrt{3}}$.

Because the lowest order problem is nonlinear, all of the higher order problems involve a linear operator $\mathcal{L}$ that is based on this front. If $U = R(z) + iI(z)$ with R and I real-valued this operator diagonalizes. That is, $\mathcal{L}(U) = \mathcal{L}_0(R) + i\mathcal{L}_1(I)$, where

$$\mathcal{L}_0 = \partial_{zz} - \frac{3}{16} + 3W_0^2 - 5W_0^4$$
$$\mathcal{L}_1 = \partial_{zz} - \frac{3}{16} + W_0^2 - W_0^4.$$

The operator $\mathcal{L}$ is self-adjoint and has three approximate null eigenfunctions. This is normal for linearizations about pulse states. We report these in the notation (R, I). The eigenfunctions consist of a phase rotation mode, $n_0 = (0, W_0)$, plus two Goldstone-type modes $n_1 = (W_{0z}, 0) = \left(\frac{\sqrt{3}}{2}\left(-B_1'B_2 + B_1B_2'\right), 0\right)$ and $n_2 = \left(\frac{\sqrt{3}}{2}\left(B_1'B_2 + B_1B_2'\right), 0\right)$. The first of these, n_1, is the *true* Goldstone mode for the pulse and is antisymmetric with respect to its center $z = 0$. This mode is inherited from global translation symmetry. Also related to translation symmetry, the mode n_2 is symmetric about the pulse center reflecting the fact that for $L \gg 1$ the two fronts are independent and can translate freely in opposite directions. This mode arises only in the limit of large L, i.e., as a result of our lowest order approximation.

The $\mathcal{O}(\epsilon)$ equation is

$$0 = \mathcal{L}(W_1) - \omega_1 W_0.$$

To enforce the solvability condition for n_2 we must require $\omega_1 = 0$. Then we may also take $W_1 \equiv 0$. At second order we obtain,

$$0 = \mathcal{L}(W_2) + \left[\left(\frac{\dot{\alpha}}{2}\right)^2 - \frac{\ddot{\alpha}}{2}z + \mu\cos\left(\frac{2\pi(z+\alpha)}{\ell}\right) - \omega_2\right]W_0.$$

The two solvability conditions can be written

$$0 = -\frac{\ddot{\alpha}}{2} I_1 - \mu \sin\left(\frac{2\pi\alpha}{\ell}\right) I_3$$
$$0 = \left[\left(\frac{\dot{\alpha}}{2}\right)^2 - \omega_2\right] I_2 + \mu \cos\left(\frac{2\pi\alpha}{\ell}\right) I_4$$

with the integrals I_k defined as follows,

$$I_1 = \langle n_1, z\, W_0 \rangle$$
$$I_2 = \langle n_2, W_0 \rangle$$
$$I_3 = \left\langle n_1, \sin\left(\frac{2\pi z}{\ell}\right) W_0 \right\rangle$$
$$I_4 = \left\langle n_2, \cos\left(\frac{2\pi z}{\ell}\right) W_0 \right\rangle.$$

Here we have used the fact that W_0 and n_2 are even functions of z while n_1 is odd to simplify the expressions.

It follows that there are only four distinct integrals to calculate. To simplify the expressions we set $c = e^{-\frac{\sqrt{3}}{4}L}$, yielding the expressions

$$I_1 = \frac{3L}{8\left(c^2-1\right)}$$
$$I_2 = \frac{6 - 3c^2\left(\sqrt{3}L + 2\right)}{8\left(c^2-1\right)^2}$$
$$I_3 = \frac{\sqrt{3}\pi^2 \mathrm{csch}\left(\frac{4\pi^2}{\sqrt{3}\ell}\right) \sin\left(\frac{\pi L}{\ell}\right)}{\ell(c^2-1)}$$
$$I_4 = -\frac{\pi \mathrm{csch}\left(\frac{4\pi^2}{\sqrt{3}\ell}\right)}{2(c^2-1)} \left(\frac{3c^2 \sin\left(\frac{\pi L}{\ell}\right)}{c^2-1} + \frac{2\sqrt{3}\pi \cos\left(\frac{\pi L}{\ell}\right)}{\ell}\right)$$
$$\approx -\frac{\sqrt{3}\pi^2 \mathrm{csch}\left(\frac{4\pi^2}{\sqrt{3}\ell}\right) \cos\left(\frac{\pi L}{\ell}\right)}{\ell(c^2-1)} + \mathcal{O}(c).$$

To obtain these expressions we have used the substitution $s = e^{\frac{\sqrt{3}}{2}z}$ followed by contour integration.

The ODEs thus take the simpler form

$$\omega_2 = \frac{\dot{\alpha}^2}{4} + \frac{\lambda L}{4} \cos\left(\frac{\pi L}{\ell}\right) \cos\left(\frac{2\pi\alpha}{\ell}\right) \tag{A3}$$
$$\ddot{\alpha} = -\lambda \sin\left(\frac{2\pi\alpha}{\ell}\right) \sin\left(\frac{\pi L}{\ell}\right), \tag{A4}$$

where $\lambda = \frac{16\sqrt{3}\pi^2\mu}{3\ell L} \mathrm{csch}\left(\frac{4\pi^2}{\sqrt{3}\ell}\right)$. It is clear from these equations that ω is slaved to the dynamics of α.

Initial conditions for the oscillators can be derived by considering the time-independent problem. Instead of using the Ansatz (A1) we seek an order-by-order expansion of the stationary localized snaking solutions. In this case α becomes time-independent and $\omega_2 \equiv 0$ but the asymptotics are otherwise unchanged. In particular since our structures are centered with respect to a cosine period we must have $\alpha = 0, \frac{\ell}{2}$; from the solvability conditions in Eqs. (A3) and (A4) it follows that we also require $L = k(\ell/2)$ with k an odd positive integer. For example, a localized state spanning 3 cosine wavelengths would have $L = 3\ell$ and $\alpha = 0$. Because the time-dependent calculation is designed to capture dynamics around perturbed stationary localized states we take $\alpha(t=0) = 0$ and $\dot{\alpha}(t=0) = 2\eta$ (the phase gradient perturbation) as initial conditions.

Before continuing to the solution of Eqs. (A4) we first discuss the role of symmetries of the original system in the ODE dynamics. The original system described by Eq. (1) possesses at least three important continuous symmetries when $m_1 = 0$. These include spatial translation $u(x,t) \to u(x+y,t)$, phase rotation $u(x,t) \to u(x,t)e^{i\theta}$, and Galilean invariance $u(x,t) \to u(x+vt,t)e^{i\frac{v}{2}\left(x+\frac{v}{2}t\right)}$. The last of these suggests that solutions traveling at a uniform velocity are not translating but rather rotating (with angular frequency $\frac{v^2}{4}$) in a moving frame. The introduction of the cosine forcing in Eq. (1) formally breaks the spatial translation and Galilean symmetries but does not preclude the existence of states that travel with *nonuniform* velocity. Indeed, it is clear from the first terms of Eq. (A3) that the Galilean structure persists for the *average* velocity of the solution. That is, if the center of mass velocity, $\dot{\alpha}$, has a nonzero time average v_{cm} then in the frame moving at this velocity the same structure has a zero average velocity but rotates in time with a frequency equal to $\frac{v_{cm}^2}{4}$.

2. ODE dynamics

We next discuss the dynamics of stationary localized states that are perturbed by a phase gradient. These states follow the dynamics of Eq. (A4) where $L = k(\ell/2)$ for an odd integer k. Changing the variables (α, τ) to new variables called (x,t), where $\alpha = \frac{\ell}{2\pi}x$ and $t = \sqrt{\frac{\ell}{2\pi\lambda}}\tau$, puts the equation of motion in canonical form,

$$\ddot{x} + \sin(x) = 0, \tag{A5}$$

and the motion reduces to that of a pendulum. There are thus two distinct dynamical regimes: libration and rotation. In the case of the solitons the libration regime corresponds to oscillations of the center of mass in space with zero mean speed while the rotation regime corresponds to propagation of solitons with nonzero mean speed. These regimes are distinguished by the value of the first integral of the equation of motion, the initial velocity, since the initial displacement is zero, $x(t=0) = 0$. Integrating Eq. (A5) once we obtain,

$$\frac{\dot{x}^2}{2} - \cos(x) = \frac{\dot{x}_0^2}{2} - 1.$$

The initial velocity can be translated back to the Ansatz variables by noticing that

$$\left.\frac{\partial x}{\partial \tau}\right|_{\tau=0} = 2\eta\sqrt{\frac{2\pi}{\ell\lambda}},$$

and is thus proportional to the magnitude of the phase gradient perturbation used in our simulations. Libration occurs when $0 < \dot{x}_0 < 2$ while rotation occurs when $\dot{x}_0 > 2$. Thus the critical transition at which solitons become "unbound" takes place at $\eta_c(\ell) = \sqrt{\frac{\lambda\ell}{2\pi}}$. In the specific cases considered here, $\ell = 10, 50$ and $\mu = 0.1$, we find $\eta_c(10) \approx \frac{0.387}{\sqrt{L}}$ and $\eta_c(50) \approx \frac{1.240}{\sqrt{L}}$.

The oscillation period in both the libration and rotation regimes may be computed in terms of elliptic integrals using standard techniques. Specifically, in the libration regime ($0 < \dot{x}_0 < 2$) there is a maximum displacement $x_{max} = 2\arcsin\left(\frac{\dot{x}_0}{2}\right) < \pi$ so the period is

$$\tilde{T}_{lib} = 4\int_0^{x_{max}} \frac{dx}{\sqrt{\dot{x}_0^2 - 4\sin^2\left(\frac{x}{2}\right)}} = 4K\left(\frac{\dot{x}_0^2}{4}\right).$$

Here $K(x)$ is the complete elliptic integral of the first kind, $K(k) \equiv \int_0^{\frac{\pi}{2}} \frac{d\theta}{\sqrt{1-k\sin^2\theta}}$, and the tilde over $\tilde{T}_{lib}$ refers to the scaled time, τ. In the rotation regime ($\dot{x}_0 > 2$) the period is defined as the time required to execute a single complete orbit,

$$\tilde{T}_{rot} = \int_0^{2\pi} \frac{dx}{\sqrt{\dot{x}_0^2 - 4\sin^2\left(\frac{x}{2}\right)}} = \frac{4}{\dot{x}_0} K\left(\frac{4}{\dot{x}_0^2}\right).$$

In the soliton context this period gives rise to the mean propagation velocity, $v_{rot} = \sqrt{\frac{\ell\lambda}{2\pi}}\frac{2\pi}{\tilde{T}_{rot}}$. In the frame moving at velocity v_{rot} the solution oscillates with period $T_{rot} = \sqrt{\frac{\ell}{2\pi\lambda}}\tilde{T}_{rot}$. The two periods computed here are plotted in Fig. 23 as a function of $\dot{x}_0$.

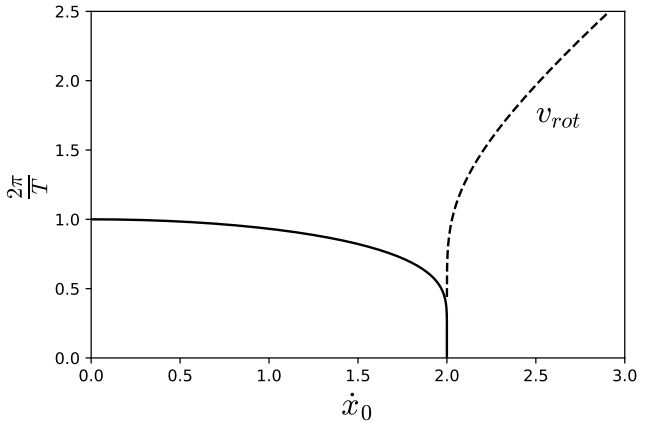

FIG. 23. The inverse periods of oscillation in the libration regime (solid line) and rotation regime (dashed line) as functions of the initial kinetic energy of the oscillator as measured by $\dot{x}_0$.

Appendix B: Numerical Implementation

1. Continuation of gap solitons

Continuation of solutions to the time-independent ODE (Eq. (2)) was performed using AUTO. AUTO discretizes the equation on an adaptive mesh and uses pseudo-arclength continuation and Newton's method in order to follow solution branches.

2. Linear stability calculations

Temporal stability calculations were performed by discretizing the linear eigenvalue problem using pseudo-spectral methods [51]. After discretization the block off-diagonal matrix eigenvalue problem for the eigenvalue σ was transformed to one of half the dimension for the eigenvalue σ^2.

As a pre-processing step for the stability calculations we transfer the ODE solutions to a uniform mesh by interpolation and then run a series of Newton iterations to increase the accuracy of the solution. Away from bifurcation points we do this using a Newton Conjugate Gradient method with preconditioning as described in [39]. The solution is approximated at 1000 points with pseudo-spectral derivatives and the Newton iterations are run until $\|\mathcal{N}(u)\|_2 \leq 10^{-14}$. Despite the comments in [52] we observe failure of this method nearby fold bifurcations. At these points the Jacobian is rank-deficient and unchecked Newton steps along its null space typically lead to divergence. We remedy this by performing a singular value decomposition of the Jacobian at each Newton update step and subtract off the projection of the Newton update along the singular vectors whose singular value falls below some threshold. At degenerate folds we typically observe that more singular values fall below the threshold as the Newton updates proceed. This method eliminates any Newton descent along the selected directions. Thus in order to optimize the accuracy of the solution it is important not to subtract off projections until the associated singular value is small. The threshold for this procedure is sensitive to the number of points in the discretization and undoubtedly the accuracy of the conjugate gradient calculations. After appropriately tuning the threshold, we observe a typical convergence to $\|\mathcal{N}(u)\|_2 \leq 10^{-11}$ using this method.

3. Time evolution simulations

Time-stepping simulations are implemented with a split-step method as described in [39]. The method in-

volves splitting the differential equation (1) into two:

$$U_t = iU_{xx}$$
$$V_t = i\left(m_0 + m_1\cos\left(\frac{2\pi x}{\ell}\right) + |V|^2 - |V|^4\right)V$$

and solving each exactly,

$$U(x,t) = \mathcal{F}^{-1}\left(e^{-ik^2t}\mathcal{F}\left(U(x,0)\right)\right) \tag{B1}$$
$$V(x,t) = V(x,0)e^{i\left(m_0+m_1\cos\left(\frac{2\pi x}{\ell}\right)+|V(x,0)|^2-|V(x,0)|^4\right)t}.$$

The time-stepping proceeds by alternate steps in time using either solution and carefully selected weighting factors. These are chosen so that the resulting method is spectrally accurate in space and fourth order accurate in time. Details can be found in [39]. Because (B1) corresponds to rotations in either real or Fourier space it preserves the L^2 norm and energy of the solution up to numerical errors. We observe good energy preservation for long simulation times.

4. Computation of the center of mass

In this section we detail the numerical implementation of the center of mass detection. A natural definition for the center of mass, $x = \alpha$, is

$$\alpha \equiv \frac{\int_\Omega xu^2\,dx}{\int_\Omega u^2\,dx}. \tag{B2}$$

On periodic domains this definition is not straightforward to implement, however. This is because the weight x in Eq. (B2) is not a periodic function. If the solution stretches across the boundary of the domain then the weight is incorrect, i.e., Eq. (B2) gives the correct center of mass on an interval but not on a circle. Solving the problem of properly weighting u to compute the center of mass on a circle is nontrivial since we only have access to a numerical sample of $u(x)$ and not the function itself, and of course we do not know α a priori. We therefore require a method that only uses integrals over $u(x)$.

These considerations lead us to propose the following method to determine α. First we define the constants A and B,

$$\begin{aligned}
A &= \int_\Omega \sin\left(\frac{2\pi x}{D}\right)u^2(x)\,dx \\
&= \cos\left(\frac{2\pi\alpha}{D}\right)\int_\Omega \sin\left(\frac{2\pi z}{D}\right)u^2(z-\alpha)\,dz - \sin\left(\frac{2\pi\alpha}{D}\right)\int_\Omega \cos\left(\frac{2\pi z}{D}\right)u^2(z-\alpha)\,dz \\
&\approx -\sin\left(\frac{2\pi\alpha}{D}\right)\int_\Omega \cos\left(\frac{2\pi z}{D}\right)u^2(z-\alpha)\,dz \\
B &= \int_\Omega \cos\left(\frac{2\pi x}{D}\right)u^2(x)\,dx \\
&= \cos\left(\frac{2\pi\alpha}{D}\right)\int_\Omega \cos\left(\frac{2\pi z}{D}\right)u^2(z-\alpha)\,dz + \sin\left(\frac{2\pi\alpha}{D}\right)\int_\Omega \sin\left(\frac{2\pi z}{D}\right)u^2(z-\alpha)\,dz \\
&\approx \cos\left(\frac{2\pi\alpha}{D}\right)\int_\Omega \cos\left(\frac{2\pi z}{D}\right)u^2(z-\alpha)\,dz\,,
\end{aligned}$$

where D is the domain length. To obtain these expressions we work in the center of mass frame and assume that the structure is approximately symmetric in this frame. This approximation is in fact implicit in the definition (B2) of the center of mass as well. Using the above expressions we define the location of the center of mass to be

$$\alpha \equiv \frac{D}{2\pi}\arctan\left(-\frac{A}{B}\right). \tag{B3}$$

This definition treats the interval $[0, D]$ as periodic and gives the correct weighting to solutions that span the boundary. We have found it to be much more accurate than Eq. (B2).

[1] D. N. Christodoulides and R. I. Joseph, Opt. Lett. **13**, 794 (1988).
[2] Z. Chen, M. Segev, and D. N. Christodoulides, Rep. Prog. Phys. **75**, 086401 (2012).
[3] Y. S. Kivshar, Opt. Lett. **18**, 1147 (1993).
[4] D. E. Pelinovsky, A. A. Sukhorukov, and Y. S. Kivshar, Phys. Rev. E **70**, 036618 (2004).
[5] I. M. Merhasin, B. V. Gisin, R. Driben, and B. A. Malomed, Phys. Rev. E **71**, 016613 (2005).
[6] G. L. Alfimov, V. V. Konotop, and P. Pacciani, Phys. Rev. A **75**, 023624 (2007).
[7] Y. V. Kartashov, V. A. Vysloukh, and L. Torner, Opt. Express **12**, 2831 (2004).
[8] Y. Zhang and B. Wu, Phys. Rev. Lett. **102**, 093905 (2009).
[9] T. J. Alexander and Y. S. Kivshar, Appl. Phys. B **82**, 203 (2006).
[10] Y. Zhang, Z. Liang, and B. Wu, Phys. Rev. A **80**, 063815 (2009).
[11] T. F. Xu, X. M. Guo, X. L. Jing, W. C. Wu, and C. S. Liu, Phys. Rev. A **83**, 043610 (2011).
[12] Z. Birnbaum and B. A. Malomed, Phys. D (Amsterdam) **237**, 3252 (2008).
[13] C. Chong, R. Carretero-González, B. A. Malomed, and P. G. Kevrekidis, Phys. D (Amsterdam) **238**, 126 (2009).
[14] J. Wang, F. Ye, L. Dong, T. Cai, and Y.-P. Li, Phys. Lett. A **339**, 74 (2005).
[15] E. M. Wright, B. L. Lawrence, W. Torruellas, and G. Stegeman, Opt. Lett. **20**, 2481 (1995).
[16] B. L. Lawrence and G. I. Stegeman, Opt. Lett. **23**, 591 (1998).
[17] F. Smektala, C. Quemard, V. Couderc, and A. Barthélémy, J. Non-Crystalline Solids **274**, 232 (2000).
[18] K. Ogusu, J. Yamasaki, S. Maeda, M. Kitao, and M. Minakata, Opt. Lett. **29**, 265 (2004).
[19] C. Zhan, D. Zhang, D. Zhu, D. Wang, Y. Li, D. Li, Z. Lu, L. Zhao, and Y. Nie, J. Opt. Soc. Am. B **19**, 369 (2002).
[20] B. C. Ponedel and E. Knobloch, Euro. Phys. J. Special Topics **225**, 2549 (2016).
[21] J. Burke and E. Knobloch, Phys. Rev. E **73**, 056211 (2006).
[22] J. Burke and E. Knobloch, Chaos **17**, 037102 (2007).
[23] R. Carretero-González, J. D. Talley, C. Chong, and B. A. Malomed, Phys. D (Amsterdam) **216**, 77 (2006).
[24] C. Taylor and J. H. P. Dawes, Phys. Lett. A **375**, 14 (2010).
[25] A. V. Yulin and A. R. Champneys, SIAM J. Appl. Dyn. Syst. **9**, 391 (2010).
[26] C. Chong and D. E. Pelinovsky, Discrete and Continuous Dyn. Syst. Ser. S **4**, 1019 (2011).
[27] A. G. Vladimirov, J. M. McSloy, D. V. Skryabin, and W. J. Firth, Phys. Rev. E **65**, 046606 (2002).
[28] J. M. McSloy, W. J. Firth, G. K. Harkness, and G.-L. Oppo, Phys. Rev. E **66**, 046606 (2002).
[29] W. J. Firth, L. Columbo, and T. Maggipinto, Chaos **17**, 037115 (2007).
[30] Y. K. Chembo, D. Gomila, M. Tlidi, and C. R. Menyuk, Euro. Phys. J. D **71**, 299 (2017).
[31] P. Parra-Rivas, D. Gomila, L. Gelens, and E. Knobloch, Phys. Rev. E **97**, 042204 (2018).
[32] D. E. Pelinovsky, *Localization in periodic potentials: from Schrödinger operators to the Gross–Pitaevskii equation*, Vol. 390 (Cambridge University Press, 2011).
[33] Y. Li, B. A. Malomed, M. Feng, and J. Zhou, Phys. Rev. A **83**, 053832 (2011).
[34] I. V. Barashenkov, Y. S. Smirnov, and N. V. Alexeeva, Phys. Rev. E **57**, 2350 (1998).
[35] P. P. Kizin, D. A. Zezyulin, and G. L. Alfimov, Phys. D (Amsterdam) **337**, 58 (2016).
[36] J. Yang, Phys. Rev. E **85**, 037602 (2012).
[37] R. L. Pego and M. I. Weinstein, Commun. Math. Phys. **164**, 305 (1994).
[38] R. L. Pego and M. I. Weinstein, Phys. Lett. A **162**, 263 (1992).
[39] J. Yang, *Nonlinear Waves in Integrable and Nonintegrable Systems* (SIAM, 2010).
[40] A. Maluckov, L. Hadžievski, and B. A. Malomed, Phys. Rev. E **77**, 036604 (2008).
[41] Y. V. Kartashov, B. A. Malomed, and L. Torner, Rev. Mod. Phys. **83**, 247 (2011).
[42] T. R. O. Melvin, A. R. Champneys, P. G. Kevrekidis, and J. Cuevas, Phys. D (Amsterdam) **237**, 551 (2008).
[43] C. Mejía-Cortés, R. A. Vicencio, and B. A. Malomed, Phys. Rev. E **88**, 052901 (2013).
[44] J. Zhou, C. Xue, Y. Qi, and S. Lou, Phys. Lett. A **372**, 4395 (2008).
[45] Y. V. Kartashov, V. A. Vysloukh, and L. Torner, Opt. Lett. **33**, 1747 (2008).
[46] Y. V. Kartashov, V. A. Vysloukh, and L. Torner, Opt. Lett. **41**, 4348 (2016).
[47] D. Pelinovsky and G. Schneider, Math. Meth. Appl. Sci. **31**, 1739 (2008).
[48] F. Haudin, R. G. Rojas, U. Bortolozzo, S. Residori, and M. G. Clerc, Phys. Rev. Lett. **107**, 264101 (2011).
[49] F. Haudin, R. G. Elías, R. G. Rojas, U. Bortolozzo, M. G. Clerc, and S. Residori, Phys. Rev. E **81**, 056203 (2010).
[50] S. Coombes and C. R. Laing, Phys. Rev. E **83**, 011912 (2011).
[51] L. N. Trefethen, *Spectral Methods in MATLAB* (SIAM, 2000).
[52] J. Yang, J. Comp. Phys. **228**, 7007 (2009).